Solid Earth

Open Access

EGU

Multiscale lineament analysis and permeability heterogeneity of fractured crystalline basement blocks

Alberto Ceccato[1,a], Giulia Tartaglia[1], Marco Antonellini[1], and Giulio Viola[1]

[1]Dipartimento di Scienze Biologiche, Geologiche ed Ambientali – BiGeA, Alma Mater Studiorum –
Università di Bologna – via Zamboni, 67, 40126 Bologna, Italy
[a]present address: Geological Institute, Department of Earth Sciences, ETH Zurich,
Sonneggstrasse 5, 8092 Zurich, Switzerland

Correspondence: Alberto Ceccato (aceccato@erdw.ethz.ch)

Abstract. The multiscale analysis of lineament patterns helps define the geometric scaling laws and the relationships between outcrop- and regional-scale structures in a fracture network. Here, we present a novel analytical and statistical workflow to analyze the geometrical and spatial organization properties of the Rolvsnes granodiorite lineament (fracture) network in the crystalline basement of southwestern Norway (Bømlo Island). The network shows a scale-invariant spatial distribution described by a fractal dimension $D \approx 1.51$, with lineament lengths distributed following a general scaling power law (exponent $\alpha = 1.88$). However, orientation-dependent analyses show that the identified sets vary their relative abundance and spatial organization and occupancy with scale, defining a hierarchical network. Lineament length, density, and intensity distributions of each set follow power-law scaling laws characterized by their own exponents. Thus, our multiscale, orientation-dependent statistical approach can aid in the identification of the hierarchical structure of the fracture network, quantifying the spatial heterogeneity of lineament sets and their related regional-vs. local-scale relevance. These results, integrated with field petrophysical analyses of fracture lineaments, can effectively improve the detail and accuracy of permeability prediction of heterogeneously fractured media. Our results also show how the geological and geometrical properties of the fracture network and analytical biases affect the results of multiscale analyses and how they must be critically assessed before extrapolating the conclusions to any other similar case study of fractured crystalline basement blocks.

1 Introduction

Crystalline rocks are characterized by very low intrinsic permeability, usually on the order of $10^{-18}\,\mathrm{m}^2$ (Achtziger-Zupančič et al., 2017; Brace, 1984), so that their capability to transmit and/or store fluids is mainly related to the structural permeability associated with fracture and fault networks created by brittle deformation and the associated fluid–rock interaction (Caine et al., 1996; Caine and Tomusiak, 2003; Ceccato et al., 2021b, a; Evans et al., 1997; Pennacchioni et al., 2016; Schneeberger et al., 2018; Stober and Bucher, 2015). When studied at different scales, fracture and fault networks commonly exhibit variable geometrical and spatial characteristics, which may significantly affect the overall permeability structure (spatial heterogeneity and anisotropy of permeable zones) of the fractured crystalline rock (Le Garzic et al., 2011; Hardebol et al., 2015; Holdsworth et al., 2019; Torabi et al., 2018). One way to obtain quantitative constraints upon the scale dependency of fracture and fault network attributes is to perform a multiscale analysis of, for example, their length and spacing distributions. The aim of these multiscale analyses is to obtain scaling laws that can quantify the variability of fracture network properties across scales (Bonnet et al., 2001; Bossennec et al., 2021; Castaing et al., 1996; Chabani et al., 2021; Dichiarante et al., 2020; Gillespie et al., 1993; McCaffrey et al., 2020; Odling, 1997).

1.1 Presentation of the problem

Quantifications across scales and scaling laws are usually derived from the analysis of lineament maps traced by remote sensing techniques (Bour et al., 2002; Castaing et al., 1996; Odling, 1997). In the past, much effort has been invested in the definition of a direct mathematical, quantitative relationship between lineament map parameters and permeability–porosity parameters (Davy et al., 2006). However, in order to provide realistic qualitative and quantitative constraints on fracture network permeability, the analysis of lineament maps requires the integration of deterministic field inputs with the geology of the remotely sensed "lineaments" (Bertrand et al., 2015; Bossennec et al., 2021, 2022; Hardebol et al., 2015). Furthermore, lineament maps provide very large and statistically robust datasets, which are, however, subject to analytical, methodological, and interpretative biases (Peacock et al., 2019; Scheiber et al., 2015). Therefore, accurate statistical analyses need to be performed to evaluate the possible biases affecting each dataset and the extrapolation limits of the observations retrieved from their analyses (Bistacchi et al., 2020; Dichiarante et al., 2020; McCaffrey et al., 2020).

1.2 Structure of the paper

In this paper, we present a methodological approach, which, when informed by statistical tests, aims to support the decision-making process during the analysis and identification of the most appropriate scaling laws describing fracture network property variability across scales, as derived from the analysis of multiscale lineament maps. In addition, we integrate previously obtained geological, geochronological, and petrophysical data about the geology and permeability of the identified lineaments to constrain the permeability structure of fractured crystalline basement units.

We describe the case study of the Bømlo crystalline basement formed by the Rolvsnes granodiorite (western Norway) (Scheiber and Viola, 2018). The lineament network detected in the Rolvsnes granodiorite developed during a prolonged brittle tectonic history within an initially massive, isotropic granitoid rock. The in situ analysis and characterization of the structural elements forming this fracture and fault zone network, e.g., the Goddo Fault Zone (GFZ, Fig. 1), have previously allowed us to reconstruct the absolute and relative timing of the various brittle deformation phases that affected the area and to quantify the geometry and petrophysical properties of the fractures (Ceccato et al., 2021b, a; Scheiber and Viola, 2018; Viola et al., 2016), although the larger-scale geometry and organization of the fracture and fault network on Bømlo remained poorly constrained and thus needed further constraining and quantification. To this end, fracture network maps of the study area were obtained from the manual picking of lineaments on lidar digital terrain model, aerial, and
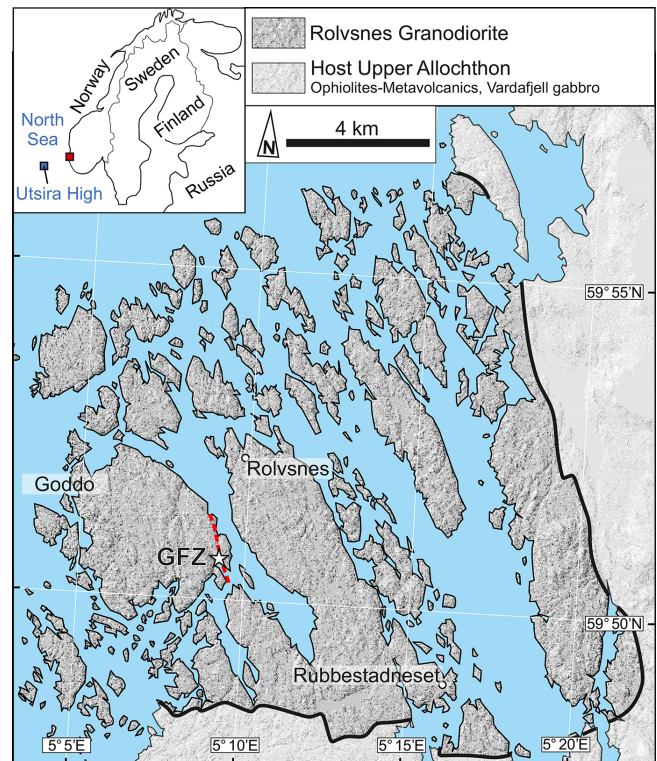

Figure 1. Simplified geological map of the part of Bømlo Island centered on the Rolvsnes granodiorite overlaying the digital terrain model obtained from a high-resolution ($1\,\mathrm{m\,pxl^{-1}}$) lidar survey (courtesy of Norges Geologiske Undersøkelse). The inset shows the location of the study area (red square) and the location of the Utsira High within the North Sea (blue square). The trace of the exposed Goddo Fault Zone (GFZ) is indicated by the red dashed line.

unmanned aerial vehicle (UAV, drone) orthophotos of the exposure area of the Rolvsnes granodiorite (Fig. 1).

The analyzed attributes include (i) fractal dimension D of the lineament network, (ii) lineament orientation, (iii) cumulative length distribution of lineaments at each analyzed scale and for each orientation set, (iv) intensity–density scaling for the whole lineament network and for each orientation set, and (v) heterogeneity of lineament spacing distribution. These parameters are usually adopted for the quantification of the spatial occupancy and of the "fractal" character of fracture–lineament networks (fractal dimension D and length distribution scaling laws), to constrain their physical connectivity and spatial organization (spacing and length) and, ultimately, for the quantification of the permeability structure of the host fractured medium (Bonnet et al., 2001; Healy et al., 2017; Nyberg et al., 2018; Peacock and Sanderson, 2018). The statistical tests adopted to constrain the most representative fitting curves and distributions include (i) least-square regression (LSR) and maximum likelihood estimation (MLE) coupled with Kolmogorov–Smirnov (KS) statistical tests adopted on cumulative distributions (Dichiarante et al.,

2020; Kolyukhin and Torabi, 2013; Rizzo et al., 2017) and (ii) bivariate box-and-whisker plots to evaluate the distribution of fracture spacing heterogeneity parameters and their statistical significance.

Our statistical, orientation-dependent multiscale analysis permits to (i) identification of groups of regional- vs. local-scale lineament sets based on the variation in geometrical and scaling parameters, (ii) definition of statistically robust scaling laws for the geometrical properties and the range of scales within which those laws can be applied, and (iii) evaluation of the difference between scaling laws retrieved from the entire network and those from individual sets. This multiscale and statistical approach tries to overcome the natural bias of lineament maps retrieved from remote sensing of natural outcrops, which are inherently incomplete due to partial exposure, resolution, and analytical biases. The implications of the adoption of general scaling laws on the upscaling and/or downscaling of fracture network properties, as well as the possible analytical biases and sources of errors in the analytical approach, are then evaluated and discussed. In this work, rather than trying to accurately quantify the scaling parameters, we focused on highlighting and analyzing the weaknesses and uncertainties that invariably accompany this sort of lineament analysis even when very robust statistical approaches and analytical methods are applied (Dichiarante et al., 2020). By integrating this information with existing field structural analyses and modeling of lineament petrophysical properties (Ceccato et al., 2021b, a; Scheiber and Viola, 2018), we provide further constraints on the multi-scale heterogeneity in magnitude, orientation, and spatial distribution of the permeability structure of the studied fractured crystalline basement.

2 Geological setting

The crystalline basement of the island of Bømlo belongs to the Upper Allochthon units of the Caledonian orogen (Gee et al., 2008). Our lineament maps represent the fracture pattern affecting the Rolvsnes granodiorite, a pre-Scandian (466 ± 3 Ma; zircon U–Pb dating) granitoid pluton hosted in the Upper Allochthon metamorphic units (Scheiber et al., 2016) (Fig. 1). The Rolvsnes granodiorite recorded a prolonged and multi-phase brittle deformation history (Scheiber et al., 2016; Scheiber and Viola, 2018), only briefly summarized in the following, while the reader is referred to the cited literature for a more detailed and comprehensive description of the tectonic history of the area. Overall, the whole tectonic history of the area is the expression of three main deformation episodes (Bell et al., 2014; Fossen et al., 2017, 2021): (1) Caledonian convergence and continental collision from the Mid-Ordovician to the Silurian, (2) extensional tectonics related to the late-Scandian orogenic collapse during the Devonian, and (3) prolonged and multi-phase extensional tectonics related to the North Sea rifting from the Permian

to the Cretaceous. During this tectonic evolution, the pre-Scandian Rolvsnes granodiorite did not record penetrative ductile strain and was instead affected by pervasive brittle deformation. Each tectonic stage recorded in the granodiorite is associated with a characteristic set of fracture and fault zones that dissect Bømlo (Scheiber and Viola, 2018): (1) NNW- and WNW-striking conjugate strike-slip faults developed coevally with ENE–WSW- and NE–SW-striking reverse faults during Caledonian convergence; (2) the same structures were reactivated with opposite kinematics during the early stages of late-Scandian orogenic collapse; (3) NW- and NNW-striking normal faults ascribable to the regional Permian-to-Jurassic rifting phase of the North Sea, which partially reactivated earlier, inherited structures. During the latest rifting stages of the North Sea, in the Early Cretaceous, new N- to NNE-striking fracture corridors and normal faults overprinted the previously formed fracture pattern. This tectonic history is reflected in the field by a sequence of three main classes of fracture and fault zones: (i) pre-Permian ESE–WNW- and NE–SW-striking mineralized shear fractures and minor faults; (ii) Permo-Jurassic major normal faults, mainly NW–SE and N–S striking; and (iii) Cretaceous fracture clusters striking N–S to NNE–SSW (Scheiber et al., 2016; Scheiber and Viola, 2018).

A key structure for the detailed analysis of the timing of deformation, the geometry of the deformation structures, and the effects of deformation on the petrophysical properties of the crystalline basement of Bømlo is the Goddo Fault Zone (GFZ, Fig. 1), (Ceccato et al., 2021b, a; Scheiber and Viola, 2018; Viola et al., 2016). The GFZ is an east-dipping normal fault that accommodated multiple slip increments during the prolonged Permian-to-Cretaceous rifting of the North Sea, recording several stages of reactivation, during which a complex network of brittle structural facies developed in the fault core (sensu Tartaglia et al., 2020). Structures like the GFZ actually controlled the permeability and fluid flow evolution from rifting to current times of the crystalline basement (Ceccato et al., 2021b, a; Viola et al., 2016).

The Rolvsnes granodiorite is interpreted as the onshore analogue of the crystalline basement of the Utsira High, which, similarly to Bømlo, is affected by a complex fracture and fault network (Fredin et al., 2017; Trice et al., 2019). The Utsira High crystalline basement is composed of (likely multiple) pre-Scandian igneous intrusions of similar age and composition to the Rolvsnes granodiorite (Lundmark et al., 2014; Slagstad et al., 2011). The fracture network in the Utsira High developed under tectonic conditions like those of the Bømlo crystalline basement, but with several significant differences mainly related to the structural position of the two crystalline basements within the North Sea rifting region (Bell et al., 2014).

3   Methods

In this study, the word "lineament" is used to refer to any linear feature of the topography as detected on a digital representation of the surface. The topography of Bømlo is cut through by deep linear grooves resulting from the penetration at depth of erosional processes exploiting fracture and fault zones of the crystalline basement (Scheiber and Viola, 2018). Therefore, the mapped lineaments represent fracture and fault zones identified in the field. In the following, the terms fracture(s) and fault zone(s) refer only to the geological structures observed in the field, which indeed assemble the remotely sensed lineaments. The lineament maps (Fig. 2a) used for the presented multiscale analyses have been generated in ArcGIS 10.8 by manually picking the same digital terrain model (DTM) of selected areas of the island of Bømlo at different scales of observation. DTMs from high-resolution ($1\,\mathrm{m\,pxl^{-1}}$) airborne light detection and ranging (lidar, kindly provided by Norges Geologiske Undersøkelse) surveys (Fig. 1) have been used for the manual picking of lineaments at the $1:5000$; $1:25\,000$ and $1:100\,000$ scales. The details of lidar data acquisition and DTMs elaboration can be found in Scheiber et al. (2015). In addition, the dataset of lineaments interpreted from the lidar DTM at the $1:5000$ scale was integrated with the interpretation of aerial orthophotos from the Bing Maps database (https://www.bing.com/maps, last access: 25 April 2022). Bing aerial imagery was also adopted to distinguish between natural and manmade linear structures and to check for artifacts and potential misinterpretation of linear features on lidar-derived DTMs in the absence of systematic ground truthing. The $1:100$ outcrop-scale lineament picking was performed on digital orthophotos of a key GFZ outcrop (Figs. 1 and 3a) as obtained from the elaboration of the imagery collected via UAV-drone surveys through structure-from-motion (SfM) algorithms. Details on this acquisition and its elaboration methods can be found in Ceccato et al. (2021a). Topographic lineaments were traced as single linear segments (not polylines) interpreting their topographic expression on DTMs. The obtained lineament maps are included in the dataset related to the present paper available at https://data.mendeley.com/datasets/3ymhkpmr9s/1 (last access: 6 September 2022). This interpretation technique introduces two major analytical biases on the obtained lineament maps: (1) the interpreted length may only partially represent the entire lineament (which may be covered by deposits or be differently expressed in the topography, thus not being visible in its entire length, e.g., Cao and Lei, 2018); (2) as a consequence, abutting relationships, intersections between lineaments, and lineament network topology and connectivity remain highly speculative and susceptible to subjective biases (Andrews et al., 2019). The orientation of mapped lineaments, expressed as azimuth angle from the geographic north, was calculated in ArcGIS 10.8 using Easy Calculate 10 (https://www.ian-ko.com/free/

free_arcgis.htm, last access: 6 September 2022) and the Orientation Analysis Tools (https://is.muni.cz/www/lenka.koc/ prvnistrana.html, last access: 6 September 2022). Rose diagrams plotting lineament azimuths were produced with the MARD 1.0 software (Munro and Blenkinsop, 2012). Lineament density P_{20} ($\mathrm{m^{-2}}$) and intensity P_{21} ($\mathrm{m\,m^{-2}}$) (Dershowitz and Herda, 1992) were calculated as the ratio between the total number of lineaments and total length of lineaments, respectively, over the total area of the land exposure in each lineament map.

3.1   Fractal dimension – box-counting method

The fractal dimension of each lineament map at different scales was computed with the box-counting method (Bonnet et al., 2001; Gillespie et al., 1993) by using the freely available function boxcount.m in MATLAB R2019b (http://www. fast.u-psud.fr/~moisy/ml/boxcount/html/demo.html, last access: 6 September 2022). The box-counting method consists in subdividing the analyzed image in progressively smaller square boxes of side b and counting how many of them contain a segment of the analyzed lineament network. Plotting the number of boxes N_b containing at least one lineament against the side length b on a log-log diagram should yield a straight curve, whose slope defines a power-law function with D as the fractal exponent (Bonnet et al., 2001). The fractal dimension obtained from the box-counting method quantifies the scaling properties of the spatial occupancy of the lineament network (Bonnet et al., 2001). We have analyzed (i) all the lineament maps at each scale of observation and, additionally, (ii) selected sub-areas of the lineament maps completely exposed on the land surface (that is, without any sea cover). Entire lineament maps inherently present discontinuous exposures of lineaments, which crop out on different islands of the Bømlo archipelago and are "separated" by sea branches and bays. Therefore, we have also analyzed the spatial occupancy (and the related fractal dimension D) of the exposed land surface of the Bømlo Island archipelago by box counting as shown in Fig. 1 in order to check if the fractal characteristics of the exposed land surface affect the fractal parameters of the fracture network. The selected areas, instead, represent continuous exposures of lineaments over several square meters or square kilometers (depending on the scale of observation). For each lineament map we have then analyzed selected areas of continuous exposure (Fig. S1 in the Supplement). For the lineament map of the GFZ outcrop we have analyzed eight sub-areas of 25 (four areas) and 100 (four areas) $\mathrm{m^2}$ each. For the $1:5000$ lineament map, we have analyzed six sub-areas of $1\,\mathrm{km^2}$ each. For the $1:25\,000$ lineament map, we have analyzed 10 sub-areas of 1 (six areas) and 4 (four areas) $\mathrm{km^2}$ each. For the $1:100\,000$ lineament map, we have analyzed four sub-areas of 4 (three areas) and 9 (1 area) $\mathrm{km^2}$ each. Selected areas and lineament maps and the complete results of the box-counting analyses are reported in Fig. S1 and in the online repository
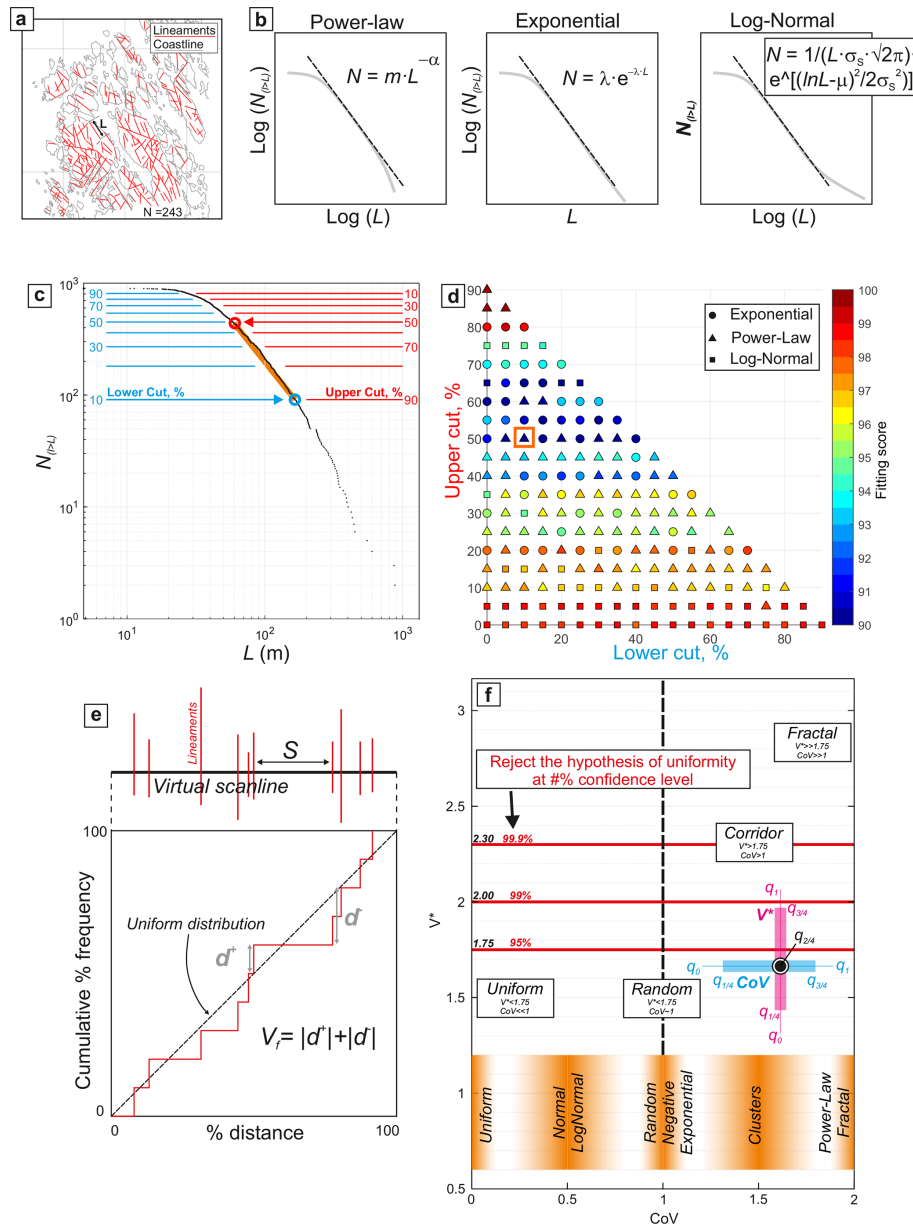
Figure 2. Explanatory figure for the Method section. **(a)** Example of lineament map retrieved from the analysis of small-scale DTMs. **(b)** Schematic representation of power law, negative exponential, and log-normal distributions, each of which defines a linear relationship between length L and cumulative number $N_{(l>L)}$ on a log-log, linear-log, or log-linear diagram, respectively. **(c)** Example of cumulative length distribution, plotted on a log-log diagram, obtained from the analysis of lineament maps explaining graphically what the upper cut and lower cut values are. The blue and red circles represent the upper and lower cut values related to the checkerboard in **(d)**. The orange segment represents the sub-domain of the cumulative distribution, included between the upper cut and lower cut bounds, fitted by the power-law relation identified by MLE–KS tests. **(c)** Example of checkerboard diagram. Each symbol (circle, triangle, square) represents a different fitting function, and each symbol is color-coded according to the fitting score yielded by the MLE–KS test for the portion of the cumulative distribution delimited by upper and lower cut values (plotted on the y and x axis, respectively). The orange square represents the results of the MLE–KS tests performed on the distribution subdomain shown in **(c)**. **(e)** Schematic representation of a virtual scanline and the related diagram showing the difference (d values) between the observed lineament distribution and a theoretical uniform (constant) distribution of spacings. **(f)** Box-and-whisker plot of coefficient of variation (CoV) vs. the statistical significance of the coefficient of heterogeneity (V^*) diagram showing the expected ranges for uniform, random, clustered, and fractal spacing distributions. The box-and-whisker plot (light blue for CoV, cyan for V^*) reports the values of the zeroth (q_0), first ($q_{1/4}$), third ($q_{3/4}$), and fourth (q_1) quartiles of the distribution of CoV and V^* results. The central dot represents the median value of the results distribution (second quartile, $q_{2/4}$).
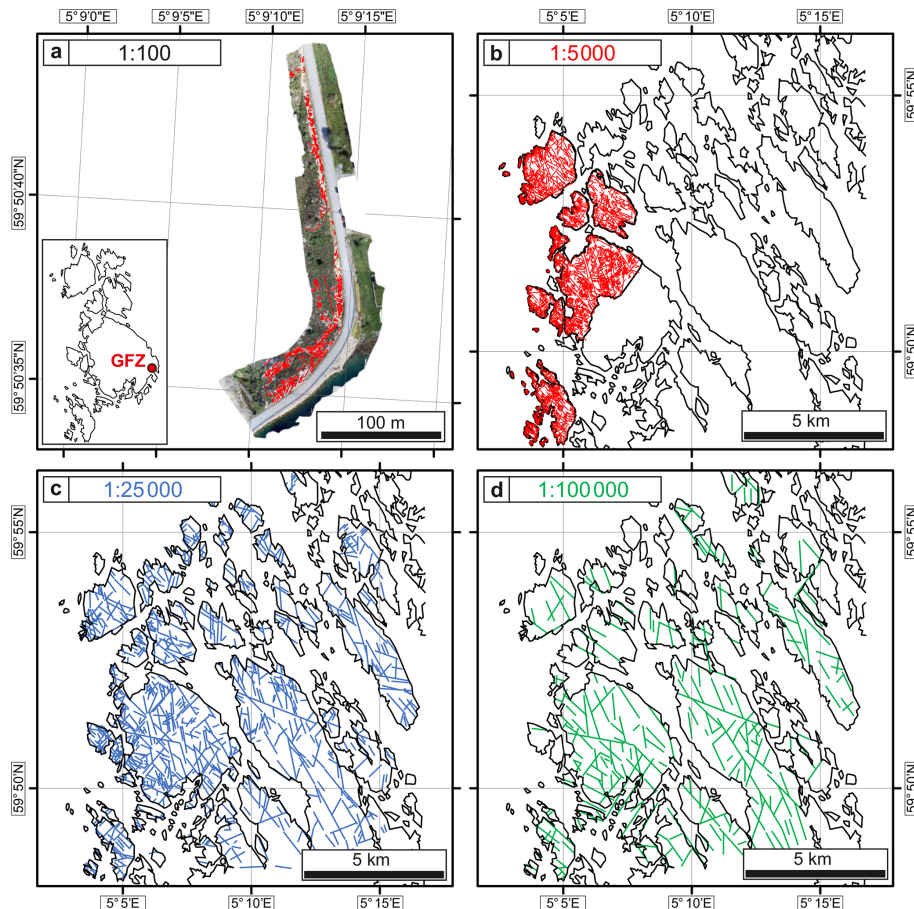
Figure 3. Lineament maps produced by manual lineament picking on outcrop orthophotos **(a)** and DTM from lidar surveys **(b–d)**.

(https://data.mendeley.com/datasets/3ymhkpmr9s/1, last access: 6 September 2022).

3.2 Cumulative length distribution analyses

Length data of lineaments have been organized as cumulative distributions and plotted in log-log diagrams of the length L of lineaments on the x axis versus $N_{(l>L)}$, the cumulative number of lineaments with length $l > L$ (Fig. 2b and c). The cumulative length distributions were then normalized by the area of the land surface reported on each map over which the lineaments were picked. Single-scale distributions report the lineament lengths at a specific scale of observation. Multiscale distributions report the sum of the cumulative length distributions observed at different scales. We have analyzed the multiscale and single-scale normalized distribution functions of (i) all lineaments included in each lineament map at different scales and (ii) each lineament orientation set at different scales.

3.2.1 Fitting of multiscale cumulative length distributions

The single-scale cumulative length distributions have been merged to form a single multiscale distribution. The mathematical functions fitting multiscale cumulative distributions are commonly retrieved by manual fitting of the distributions by assessing the slope of the tangent to the observed distributions (e.g., Bertrand et al., 2015; Bossennec et al., 2021; Castaing et al., 1996; Le Garzic et al., 2011). Here we apply a more quantitative method by adopting least-square regression (LSR) in Microsoft Excel to the multiscale cumulative distributions. Manual fitting has been performed as well (results are reported and compared to LSR fitting in Fig. S2 in the Supplement).

3.2.2 Fitting of single-scale cumulative length distributions

Single-scale cumulative length distributions have been analyzed by means of the maximum likelihood estimation (MLE) and Kolmogorov–Smirnov (KS) statistical tests to retrieve the best fitting mathematical function (Dichiarante et

al., 2020; Kolyukhin and Torabi, 2013; Rizzo et al., 2017). The mathematical functions considered were negative exponential, power-law, and log-normal (Fig. 2b). The advantage of adopting MLE–KS statistical tests derives from the possibility to also retrieve the function parameters (namely the exponent λ for the exponential, the exponent α for the power-law, and the mean μ and standard deviation σ for the log-normal functions) in addition to the mathematical function best approximating the observed cumulative length distributions. A dedicated MATLAB script implementing the freely available functions provided in the latest version of Frac-PaQ (Healy et al., 2017; Rizzo et al., 2017) was used for this purpose. The results of the MLE–KS tests are reported in "checkerboard" diagrams, following the method proposed by Dichiarante et al. (2020) (Fig. 2d). Such diagrams allow us to image the results of the MLE–KS tests on the selected portions of the cumulative distribution, i.e., the best fitting mathematical function for varying subdomains of the cumulative distribution. A subdomain is defined as a segment of the cumulative distribution curve bounded by a lower and upper cut value (Fig. 2c and d). The upper cut (UC) value represents the distance, expressed in terms of percentage of the total number of elements contained in the cumulative distribution, from the shortest observed length. The lower cut (LC) value represents the distance, in terms of percentage of the total number of elements contained in the cumulative distribution, from the longest observed length. On the checkerboard diagrams, the LC values are plotted versus the UC values (Fig. 2d). Each point of the checkerboard represents a specific percentage range of the total cumulative distribution between the upper and lower cut limits over which the MLE–KS tests were run. The plotted symbol represents the mathematical function among those considered (power-law, exponential, log-normal) for which the MLE–KS tests yielded the highest fitting score, whereas the symbol is color-coded according to the retrieved value of the fitting scores (namely the H percentage (HP) and the P percentage (PP) parameters; see Rizzo et al., 2017; Dichiarante et al., 2020). This analytical approach allows for the determination of the mathematical function that best fits the truncated cumulative distribution and for the evaluation of the effects of truncation and censoring biases (Fig. 2c and d). We report in the main text and tables the range of UC values for which each function fits best: the upper cut values quantify the "truncation" of the cumulative distribution at short lengths, and this has been demonstrated to deeply affect the results of MLE–KS tests (Dichiarante et al., 2020).

3.3 Spatial distribution analysis

The spatial distribution of lineaments has been quantified following the approach by Sanderson and Peacock (2019). We analyzed the spacing between lineaments collected along virtual scanlines computed with the NetworkGT toolkit in QGis 3.12.2 (Nyberg et al., 2018) (e.g., Fig. 2e). The lin-

eaments were classified and grouped into orientation sets. A grid of equally spaced virtual scanlines (100 m spacing for the 1 : 5000 scale and 500 m spacing for the 1 : 25 000 and 1 : 100 000 scales) oriented perpendicular to the selected lineament set orientation was drawn upon the imported lineament map with NetworkGT (e.g., Fig. 2e). Intersections between each virtual scanline and map lineament were also obtained in NetworkGT. For each scanline, we analyzed the statistics (mean – μ, standard deviation – σ_S, and minimum and maximum values) for several parameters (Fig. 2e): (i) spacing (S) between lineaments; (ii) coefficient of variation (CoV) of the spacing, defined as the ratio between the standard deviation of spacing along a scanline and its average (CoV $= \sigma_S/\mu$) (Gillespie et al., 2001); and (iii) coefficient of heterogeneity (V_f) and its statistical significance (V^*) according to Sanderson and Peacock (2019). The CoV of spacing is commonly adopted to assess the spatial organization (clustering vs. uniform distribution) of lineaments along scanlines (e.g., Gillespie et al., 2001). CoV values > 1 are usually related to clustered lineaments; CoV $= 1$ should represent a (negative) exponential-random distribution of spacing intervals, and CoV < 1 is usually related to log-normal (uniform) spacing distributions (Gillespie et al., 2001; McCaffrey et al., 2020; Odling et al., 1999). The spacing heterogeneity, i.e., the deviation of the spacing distribution along a scanline from a uniform distribution, is quantified by the V_f and V^* coefficients computed with the Kuiper method (Sanderson and Peacock, 2019). The coefficient of heterogeneity V_f quantifies the deviation from a theoretical uniform distribution of the observed spacing distribution along a given scanline expressed as the sum of the moduli of the positive and negative deviations (see Sanderson and Peacock, 2019; Fig. 2e). The coefficient V^* quantifies the statistical significance of the heterogeneity factor V_f:

$$V^* = V_f \left(\sqrt{N_i} + 0.155 + \frac{0.24}{\sqrt{N_i}} \right), \tag{1}$$

where N_i represents the number of lineaments intersected by the scanline. Stephens (1970) demonstrated that for $V^* >$ 1.75, 2.0, and 2.3, the null hypothesis of uniformity can be rejected at the 95 %, 99 %, and 99.9 % levels, respectively. Thus, the coefficient V^* can be used to quantify the probability that a certain spacing distribution is uniform or not.

We present the results of this analyses as CoV–V^* diagrams (Fig. 2f) in which we plot the statistical distribution of the values of CoV vs. V^* as box-and-whisker plots. In doing so, we can qualitatively evaluate if, statistically, a set of lineaments has a random or organized spatial distribution (Sanderson and Peacock, 2019). With this method, four main spatial organization types can be distinguished (Fig. 2f): (i) uniform distribution, characterized by CoV $\ll 1$ and $V^* <$ 1.75; (ii) random distribution, characterized by CoV ≈ 1 and $V^* < 1.75$; (iii) corridor/clustered distribution, characterized by CoV > 1 and $V^* > 1.75$–2.00; (iv) fractal distribution, characterized by CoV $\gg 1$ and $V^* \gg 1.75$–2.00. Scanlines

with more than 10, 5, and 3 lineament intersections were considered on maps at 1 : 5000, 1 : 25 000, and 1 : 100 000, respectively.

Given the limited number of intersections recorded by each virtual scanline in our maps ($N_i \ll 30$), more advanced and up-to-date analyses of the spacing variability (Marrett et al., 2018; Sanderson and Peacock, 2019; Bistacchi et al., 2020) were not possible. The Vf-V^* method proposed by Sanderson and Peacock (2019) yields statistically meaningful results for datasets containing a number of intersected lineaments $N_i > 6$. Our datasets unfortunately do not always satisfy this requirement. To perform the analysis on a statistically meaningful number of samples (total number of scanlines, $N_{SL} > 10$), we had to reduce the minimum number of spacing data each scanline had to contain to be included in the dataset. Therefore, our analyses report the results from scanlines showing a minimum number of intersections $N_i > 10$, > 5, and > 3 for the analyses performed at the 1 : 5000, 1 : 25 000 and 1 : 100 000 scale, respectively.

All parameters and the related abbreviations are reported in Table 1.

4 Results

4.1 Lineament map description

The manual picking of topographic lineaments on different digital representations of the selected areas of Bømlo led to the production of maps at different scales (Figs. 3 and S1, S3, and S4 in the Supplement). The orthophotos retrieved from UAV-drone surveys and the related lineament map (Figs. 3a and S3a) helped to characterize the main outcrop of the GFZ along the eastern shoreline of Goddo Island (Ceccato et al., 2021b, a; Viola et al., 2016). The investigated areas extend for 2127 m^2, over which we picked 930 lineaments. Lineament mapping on lidar DTM and aerial imagery at the 1 : 5000 scale (Figs. 3b and S3b) was performed on the best exposed areas along the coastline of Goddo Island and nearby smaller islands. The resulting lineament map covers more than 17 km^2 and includes 3835 lineaments. Furthermore, we generated additional lineament maps from the interpretation of the lidar DTM at the 1 : 25 000 and 1 : 100 000 scales over the same area (83 km^2; Figs. 3c and d and S3c and d). The 1 : 25 000 lineament map contains 894 lineaments, whereas the 1 : 100 000 map contains 249 lineaments.

4.2 Fractal dimension

The fractal dimension of the lineament maps at all scales was evaluated by applying the box-counting method (Bonnet et al., 2001; Gillespie et al., 1993). The number of filled boxes N_b decreases with increasing box size b following a power-law relationship (Fig. 4). The power-law exponents (the fractal exponents) retrieved from the box-counting analyses of the entire lineament maps at different scales range

Table 1. Summary table of the parameters and related nomenclature adopted in this paper.

Parameter		Unit
μ	Mean	–
σ_S	Standard deviation	–
R^2	Coefficient of determination	–
m	Proportionality coefficient for scaling laws	–
s	Scale	–
b	Box size for box counting	m
N_{Lin}	Number of lineaments	–
N_b	Number of filled boxes	–
$N_{(l>L)}$	Number of lineaments with a length $l > L$	–
N_i	Number of lineaments intersected by a scanline	–
N_{SL}	Number of scanlines	–
L	Length of lineaments	m
D	Fractal dimension	–
P_{20}	Lineament–fracture density	m^{-2}
P_{21}	Lineament–fracture intensity	m m^{-2}
S	Spacing	m
α	Exponent of power-law distribution	–
β	Exponent of density scaling law	–
δ	Exponent of intensity scaling law	–
λ	Exponent of negative exponential distribution	m^{-1}
Xmin	Minimum lineament length of the truncated dataset	m
UC	Upper cut	%
LC	Lower cut	%
HP	H percentage	%
PP	P percentage	%
CoV	Coefficient of variation for spacing	–
d	Difference from uniform distribution	%
V_f	Coefficient of heterogeneity	–
V^*	Statistical significance of coefficient V_f	–

between 1.45 and 1.61 (Fig. 4). On average, the lineament network exposed on the discontinuous outcrops of the Bømlo island archipelago is characterized by a fractal dimension $D = 1.51 \pm 0.14$ ($2\sigma_S$). The analysis of the spatial occupancy of the exposed land surface of the Bømlo island archipelago yielded a fractal dimension $D = 1.72$ (Fig. 4; see supplementary dataset in the online repository).

Figure 4 shows the box-and-whisker diagram of the fractal exponent D for each scale of observation as obtained from the analyses of selected areas. The fractal dimensions D obtained from the analyses of both entire lineament maps (cross marker in Fig. 4) and selected areas (box-and-whisker plots in Fig. 4) are always smaller than the fractal dimension D of the exposed land surface on the Bømlo island archipelago ($D = 1.72$; gray solid line in Fig. 4). Similarly, the fractal dimension of the whole lineament maps at 1 : 5000, 1 : 25 000,
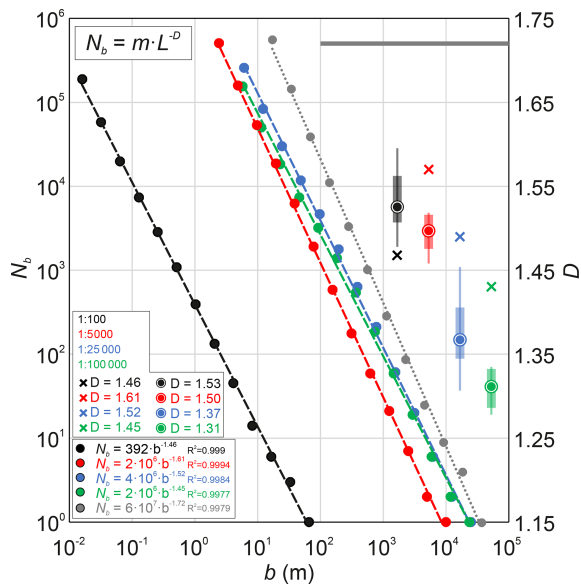
Figure 4. Results of the box-counting method applied to the lineament maps of Fig. 3. The dashed interpolation curves represent the results from box-counting analyses of the entire lineament maps for each scale of observation. The gray dotted curve represents the results of the box-counting analyses applied to the distribution of the exposed land surface in the Bømlo island archipelago. The solid gray line represents the value of D for the land surface ($D = 1.71$). The box-and-whisker plot represents the distribution of the fractal dimension D obtained from the box-counting analyses of selected sub-areas of lineament maps for each scale of observation. Encircled dots represent the average value of D obtained from the analyses of sub-areas. The cross marker represents the fractal dimension D obtained from the analysis of the entire lineament map (lineaments maps and selected sub-areas are reported in Fig. S1; the whole dataset is available at the online repository).

and $1:100\,000$ scales always over-estimate the fractal dimensions D obtained from the analyses of selected areas. This is not true for the GFZ lineament map at the $1:100$ scale, in which the average fractal dimension of the considered sub-areas is systematically larger than that of the entire lineament map ($D = 1.46$). The distribution of D values from sub-areas from the $1:100$ and $1:5000$ scales overlaps and is very similar from a statistical point of view ($D > 1.46$). Similarly, the sub-areas of the $1:25\,000$ and $1:100\,000$ scales yielded similar distributions of D ($D < 1.45$).

4.3 Lineament orientation

The comparison of the rose diagrams at different scales of observation allows the definition of some dominant trends (Fig. 5a and b). The five main orientation sets are (Figs. 5a and S4 and Table 2) (a) a N–S-striking Set 1, (b) a NE–SW-striking Set 2, (c) a ENE–WSW-striking Set 3, (d) a ESE–WNW-striking Set 4, and (e) a SE–NW-striking Set 5. These sets display a significant variation in their rela-
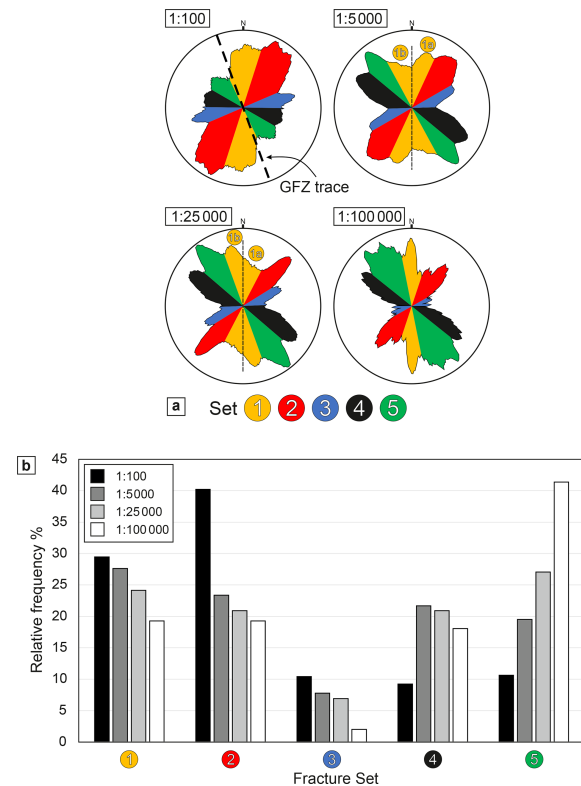

Figure 5. Rose diagrams **(a)** and histograms of the relative frequencies **(b)** of the identified orientation sets at different scales of observation.

tive abundance across scales. At the smallest scale of observation ($1:100\,000$), Set 5 is dominant, whereas at the largest observation scale ($1:100$), Sets 1 and 2 are dominant (Fig. 5b). At intermediate scales ($1:5000$; $1:25\,000$), all sets are equally represented (Table 2). Set 3 is the least represented, occurring only in small percentages ($< 10\,\%$) at all scales (Table 2). Sets 2 to 5 have a constant average orientation across scales, but the average orientation of Set 1 lineaments changes with scale of observation. N–S-striking orientations are dominant at the smallest and largest scales of observation. At the intermediate scale, Set 1 presents either a NNW- (scale $1:5000$) or a NNE-dominant strike (scale $1:25\,000$) (Fig. 5a). Therefore, we have subdivided Set 1 into Set 1a, including NNE–SSW-striking lineaments, and Set 1b, including N–S- to NNW–SSE-striking lineaments. This subdivision will be adopted for discussing the spatial organization of the lineaments.

4.4 Cumulative length distributions

The results of LSR fitting and MLE–KS tests are reported and summarized in Fig. 6 and Table 3; the checkerboard diagrams are reported in the Supplement (Fig. S5 in the Supplement).

Table 2. Table presenting the orientation data for the identified lineament sets for each scale of observation. Azimuth (°) represents the average strike of the manually picked lineaments. Total L represents the sum of the length of all picked lineaments in each map for each set.

	Set	Azimuth (°)	N_{Lin}	Relative frequency (%)	P_{20} (m^{-2})	Total L (m)	P_{21} (m m^{-2})
s				1 : 100			
Area (m^2)	1	0–17; 156–180	274	29.46	1.29×10^{-1}	490.10	2.30×10^{-1}
2127	2	19–67	374	40.22	1.76×10^{-1}	771.86	3.63×10^{-1}
	3	68–91	97	10.43	4.56×10^{-2}	156.25	7.35×10^{-2}
	4	92–120	86	9.25	4.04×10^{-2}	134.12	6.31×10^{-2}
	5	121–155	99	10.65	4.65×10^{-2}	175.30	8.24×10^{-2}
	Total		930		4.37×10^{-1}	1727.63	8.12×10^{-1}
s				1 : 5000			
Area (m^2)	1	0–28; 154–180	1059	27.61	6.17×10^{-5}	103 655.02	6.04×10^{-3}
17 170 533	2	29–60	896	23.36	5.22×10^{-5}	76 172.72	4.44×10^{-3}
	3	61–88	299	7.80	1.74×10^{-5}	23 934.34	1.39×10^{-3}
	4	89–130	832	21.69	4.85×10^{-5}	80 080.14	4.66×10^{-3}
	5	131–153	749	19.53	4.36×10^{-5}	90 759.34	5.29×10^{-3}
	Total		3835		2.23×10^{-4}	374 601.56	2.18×10^{-2}
s				1 : 25 000			
Area (m^2)	1	0–25; 162–180	216	24.16	2.60×10^{-6}	93 912.71	1.13×10^{-3}
83 000 724	2	26–59	187	20.92	2.25×10^{-6}	60 252.45	7.26×10^{-4}
	3	60–90	62	6.94	7.47×10^{-7}	20 544.88	2.48×10^{-4}
	4	91–131	187	20.92	2.25×10^{-6}	74 024.49	8.92×10^{-4}
	5	131–161	242	27.07	2.92×10^{-6}	113 476.26	1.37×10^{-3}
	Total		894		1.08×10^{-5}	362 210.79	4.36×10^{-3}
s				1 : 100 000			
Area (m^2)	1	0–19; 171–180	48	19.28	5.78×10^{-7}	35 972.83	4.33×10^{-4}
83 000 724	2	20–60	48	19.28	5.78×10^{-7}	38 877.02	4.68×10^{-4}
	3	61–90	5	2.01	6.02×10^{-8}	4354.50	5.25×10^{-5}
	4	91–130	45	18.07	5.42×10^{-7}	36 742.25	4.43×10^{-4}
	5	131–171	103	41.37	1.24×10^{-6}	106 590.06	1.28×10^{-3}
	Total		249		3.00×10^{-6}	222 536.66	2.68×10^{-3}

The results of the MLE–KS tests suggest that a log-normal function best approximates the entire single-scale distribution in all considered cases (Fig. S5 and Table 3). Variably truncated distributions are best approximated by either negative exponential or power-law functions (Table 3). In particular, the truncated length probability distributions for both single sets and the entire lineament network mapped at 1 : 100 are best represented by negative exponential functions, with λ ranging between 0.65 and 1.25. Truncated distributions retrieved from lineament maps at 1 : 5000 are best fitted, in most cases, by power-law functions with a minimum exponent α of 2.2. Truncated length distributions for lineaments mapped at 1 : 25 000 and 1 : 100 000 scales are well approximated by negative exponential functions, with an average λ of 0.004 and 0.0017, respectively (Table 3).

Figure 6a reports the cumulative length distributions for the entire set of lineament maps normalized to the area of investigation at each scale of observation. The multiscale normalized cumulative distributions obey a general power-law relationship valid over 5 orders of magnitude (1 to 10 000 m). The power-law exponent α is 1.88 (Fig. 6a). Figure 6b reports the multiscale cumulative length distributions for each lineament set normalized for the area of investigation. Also in this case, multiscale distributions obey a general power-law scaling with a characteristic exponent α for each set ranging between 1.62 and 2.12 (Figs. 6b and S2).

4.5 Lineament density and intensity

As also suggested by the cross-scale variation in the relative proportions of the orientation sets (Fig. 5a and b), the normalized density P_{20} (m^{-2}) and intensity P_{21} (m m^{-2}) of

Table 3. Summary table of MLE–KS test results on distribution fitting. The table reports only results of the analyses of datasets containing a significant number of lineaments ($N_{Lin} \geq \sim 50$). Fitting score: value of the HP parameter obtained from the MLE–KS tests. Range (UC %): range of upper cut values within which the fitting score is at a maximum for the selected fitting function. Xmin: minimum length above which the fitting is performed, corresponding to the lower bound of the range of upper cut values.

s	Set	N_{Lin}	L min (m)	L max (m)	Mean L (m)	Exponential				Power law				Log-normal			
						Fitting score	Range (UC %)	λ	Xmin (m)	Fitting Score	Range (UC %)	α	Xmin (m)	Fitting Score	Range (UC %)	μ	σ_S
1 : 100	1	274	0.3	6.9	1.8	> 90	40–90	1.05–1.25	> 1.4	–	–	–	–	> 90	0–35	0.45–0.75	0.52–0.37
	2	374	0.3	8.7	2.1	> 90	> 10	0.65–0.79	> 0.9	–	–	–	–	> 90	0–5	0.55–0.65	0.55–0.57
	3	95	0.4	5.6	1.6	> 90	10–65	0.95–1.05	0.8–1.8	> 90	70–85	3.8–5	1.9	> 90	0–5	0.35–0.45	0.5–0.55
	4	86	0.3	5.0	1.6	> 90	> 50	1.05–1.25	> 1.25	–	–	–	–	> 90	0–45	0.25–0.75	0.35–0.65
	5	99	0.3	10.7	1.8	> 90	15–65	0.90–1.05	0.9–2.0	> 90	> 70	4.25–4.75	2.1	> 90	0–10	0.4–0.5	0.46–0.55
	Total	930	0.3	10.7	1.9	> 90	15–60	0.78–0.82	1.2–2.0	> 90	> 65	3.6–4.1	2.1	> 90	0–10	0.45–0.65	0.51–0.59
1 : 5000	1	1059	14.4	1759.3	97.9	< 90	15–20	0.013	40–50	> 90	> 25	2.2–3.1	50	< 90	0–10	4.3–4.5	0.63–0.72
	2	896	4.8	1315.6	85.0	< 90	10–20	0.016	40	> 90	> 25	2.4–3.2	50	< 90	0–5	4.25	0.67–0.70
	3	299	5.3	1265.5	80.0	< 90	10–20; 40–55	0.017; 0.015	40; 60	< 90	25–35; > 60	2.6; 2.8–3.4	50; > 60	> 90	0–5	4.2	0.65–0.7
	4	832	8.1	1014.3	96.3	< 90	10–40; 55–65	0.013; 0.0115	45; 80	< 90	45–55; > 70	2.6; 2.9	50; 90	> 90	0–5	4.3	0.7
	5	749	11.8	2306.4	121.2	< 90	25	0.01	60	< 90	> 30	2.4–2.8	70	< 90	0–20	4.5–4.8	0.65–0.77
	Total	3791	4.8	2306.4	97.9	–	–	–	–	< 90	> 45	2.4–3.2	70	< 90	0–40	4.3–4.7	0.55–0.75
1 : 25 000	1	216	88.7	1681.5	434.8	> 90	> 5	0.0036–0.0043	200	–	–	–	–	> 90	0–5	5.5–6	0.45–0.55
	2	187	61.2	1264.1	322.2	> 90	> 10	0.0045–0.0052	175	–	–	–	–	> 90	0–5	5.6–5.7	0.54–0.57
	3	62	105.0	1678.7	331.4	> 90	0–10; > 75	0.0045; 0.003	125; 275	> 90	15–70	2.6–2.9	150	–	–	–	–
	4	187	79.0	2652.4	395.9	> 90	10–70	0.0038–0.004	200–400	> 90	> 75	3.6–3.8	425	> 90	0–5	5.8–5.9	0.55–0.57
	5	242	89.9	1946.3	468.9	> 90	5–75	0.0032–0.0037	250	> 90	> 80	3.8–4.6	600	> 90	0	6	0.55
	Total	894	61.2	2652.4	405.2	> 90	> 10	0.0034–0.004	200	–	–	–	–	> 90	0–5	5.8–6	0.55–0.57
1 : 100 000	1	48	312.5	1892.8	749.4	> 90	> 35	0.0029–0.0034	650	–	–	–	–	> 90	0–30	6.5–6.7	0.34–0.41
	2	48	226.2	2683.6	809.9	> 90	0–15; 30–90	0.0016–0.0019	300	–	–	–	–	> 90	20–25	6.7	0.5
	3	5	400.4	1586.0	870.9	–	–	–	–	–	–	–	–	–	–	–	–
	4	45	208.5	3936.9	816.5	–	–	–	–	–	–	–	–	–	–	–	–
	5	103	250.0	3224.7	1034.9	> 90	> 15	0.0016–0.0018	300	–	–	–	–	> 90	0–10	6.8–6.9	0.47–0.55
	Total	249	208.5	3936.9	893.7	> 90	> 10	0.0017–0.00185	400	–	–	–	–	> 90	0–5	6.7–6.8	0.5–0.55

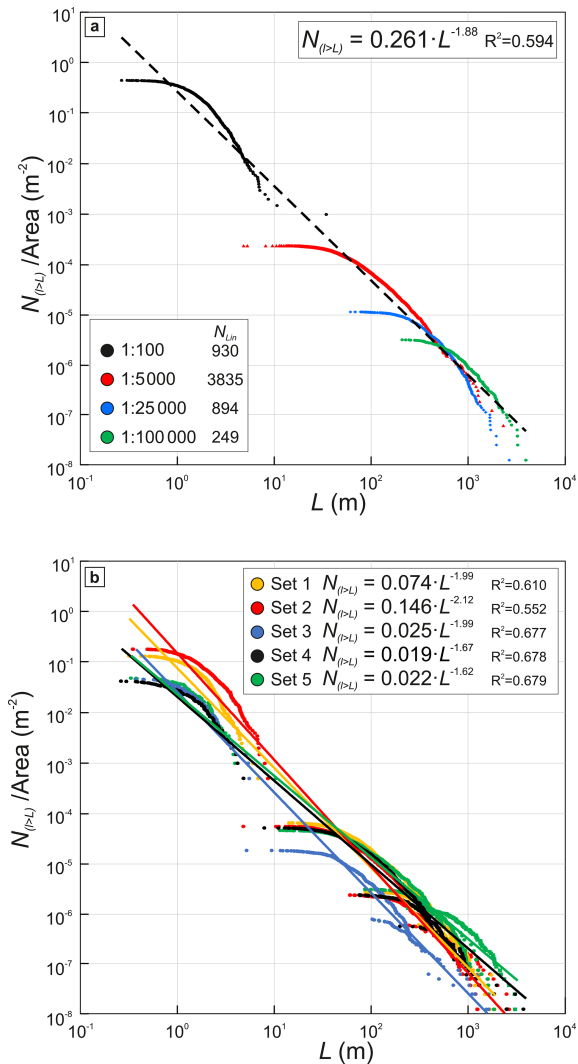$$N_{(l>L)} = 0.261 \cdot L^{-1.88} \quad R^2 = 0.594$$

Figure 6. (a) Log-log diagram of lineament length L vs. cumulative number of lineaments $N_{(l>L)}$ per unit area showing the cumulative length distribution for the lineament maps reported in Fig. 3. (b) Log-log diagram as above showing the cumulative length distribution for each orientation set.

each lineament set vary across scales. The variations in density and intensity are both described by a power-law relationship in log-log diagrams plotting the scale on the x axis (e.g., $10^5 = 1 : 100\,000$) and the density P_{20} or intensity P_{21} on the y axis (Fig. 7a and b) (e.g., Castaing et al., 1996). The variation trend for the total lineament density P_{20} of each map at different scales is characterized by power-law exponents $\beta = 1.77$ (Fig. 7a). Sets 1–3 display β values larger than the average value; Sets 4 and 5 display β values smaller than the average values. Similarly, the variation trend for P_{21} is characterized by a power-law exponent $\delta = 0.86$ (Fig. 7b); Sets 1–3 show δ values larger than the average value. Sets 4 and 5 display δ values smaller than the average value.

4.6 Spacing and organization at different scales

The CoV–V^* diagrams highlight a similar trend for all analyzed lineament sets with an increasing scale of observation (from $1 : 100\,000$ to $1 : 5000$). At the $1 : 5000$ scale (Fig. 8a), Set 1a and 1b lineaments are characterized by CoV ≤ 1 and $V^* \leq 1.75$, suggesting a random-to-uniform spatial distribution. At smaller scales, CoV for Set 1 exhibits a tendency towards random-to-uniform distribution (Fig. 8b and c). Set 2 lineaments display CoV on average > 1 at the $1 : 5000$ scale and $V^* > 1.75$ for a significant number of data ($> 40\,\%$ of the total number of data), suggesting a clustered spatial distribution. At smaller scales, both CoV and V^* values generally decrease, although some of the analyzed scanlines still display CoV > 1 and $V^* > 1.75$–2.00. Set 3 lineaments are too scattered and sparse to allow for a meaningful analysis of their spatial arrangement, and, therefore, they are not reported in Fig. 8. Set 4 lineaments mapped at the $1 : 5000$ scale on average show CoV values > 1, but V^* is rarely > 1.75. At smaller scales, both CoV and V^* decrease progressively. CoV and V^* for Set 5 lineaments are generally < 1 and < 1.75, respectively. The most significative variation across scales in spatial distribution occurs for Set 2 and Set 4, both of which exhibit a tendency towards clustering at the large scale ($1 : 5000$; CoV > 1, $V^* > 1.75$; Figs. 8a–9d), whereas they exhibit a tendency toward a random-to-uniform distribution at the smaller scales ($1 : 25\,000$ and $1 : 100\,000$; CoV < 1; $V^* < 1.75$; Figs. 8b and c and 9e). None of the lineament sets show a tendency to develop fractal behavior with a power-law spacing distribution.

5 Discussion

In the following, we first assess the geometrical characteristics, scaling laws, and exponent values obtained for the Rolvsnes granodiorite fracture network. Then, we evaluate the possible biases affecting the analyzed datasets and their effect on the quantification of the fracture network geometrical properties. In addition, we discuss the implications of applying the scaling relationships to the quantification of fracturing and reservoir permeability at different scales by integrating our results with field geological data.

5.1 Characterization of geometric properties of the Rolvsnes granodiorite lineament network

The fractal dimensions D retrieved from the analysis of the 2D entire lineament maps cluster around 1.5 (Fig. 4), similar to what is commonly reported from other case studies on lineament pattern fractal dimensions (Bonnet et al., 2001; Hirata, 1989). Also, the normalized cumulative distribution of lineament lengths effectively defines a single scaling law, which can be best described by a power-law relationship with an exponent $\alpha = 1.88$ (Fig. 6a and Table 5). The general scaling law obtained for the overall lineament network
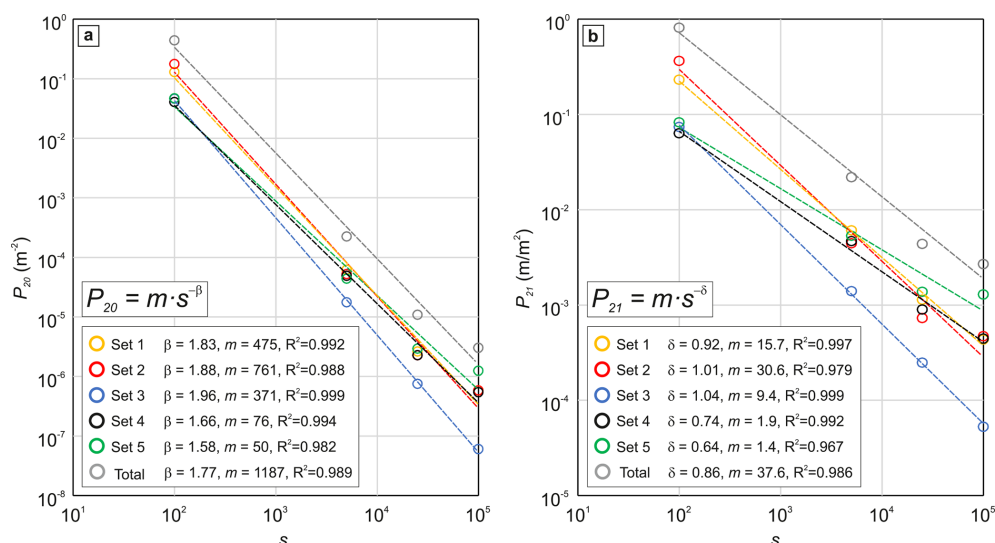
Figure 7. Lineament density (P_{20}) and intensity (P_{21}) variation across scales for each orientation set (Sets 1 to 5) and for the entire lineament network (total).
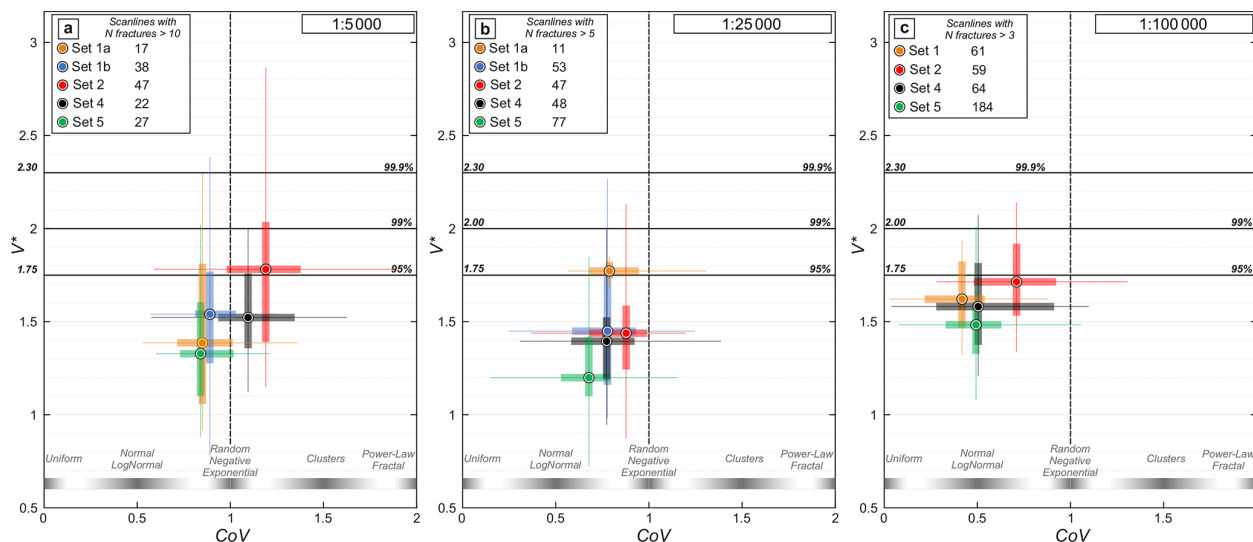

Figure 8. Box-and-whisker plots reporting CoV–V^* values quantifying the spatial organization of the orientation sets identified in the lineament map at **(a)** 1 : 5000, **(b)** 1 : 25 000, and **(c)** 1 : 100 000 scales.

is very similar to that derived from many other case studies of fracture networks affecting both crystalline basements and (meta)sedimentary rocks, with an average power-law exponent close to $\alpha = 2$ (see Bertrand et al., 2015; Bonnet et al., 2001; Bossennec et al., 2021; Chabani et al., 2021; Le Garzic et al., 2011; McCaffrey et al., 2020; Odling, 1997; Torabi and Berg, 2011). The power-law scaling relationship defined by the lineament density P_{20} values is characterized by a power-law exponent $\beta = 1.77$, similar to the value of 1.7 commonly observed in many other fault networks (Castaing et al., 1996; Bonnet et al., 2001, and references therein).

5.1.1 Scale-invariant lineament network

A similar fractal dimension D and power-law scaling relationship are commonly used as evidence for the occurrence of a fracture network whose geometrical properties (size of fractures, i.e., length and spatial correlation and organization) are scale-invariant (Bonnet et al., 2001). This suggests that, at a first approximation, the documented lineament pattern in the Rolvsnes granodiorite is self-similar at any scale of observation. However, the Rolvsnes granodiorite case appears to be more complex than it would seem at a first glance. The detailed analyses of lineament maps, fractal dimension D, and the geometrical properties of orientation sets revealed
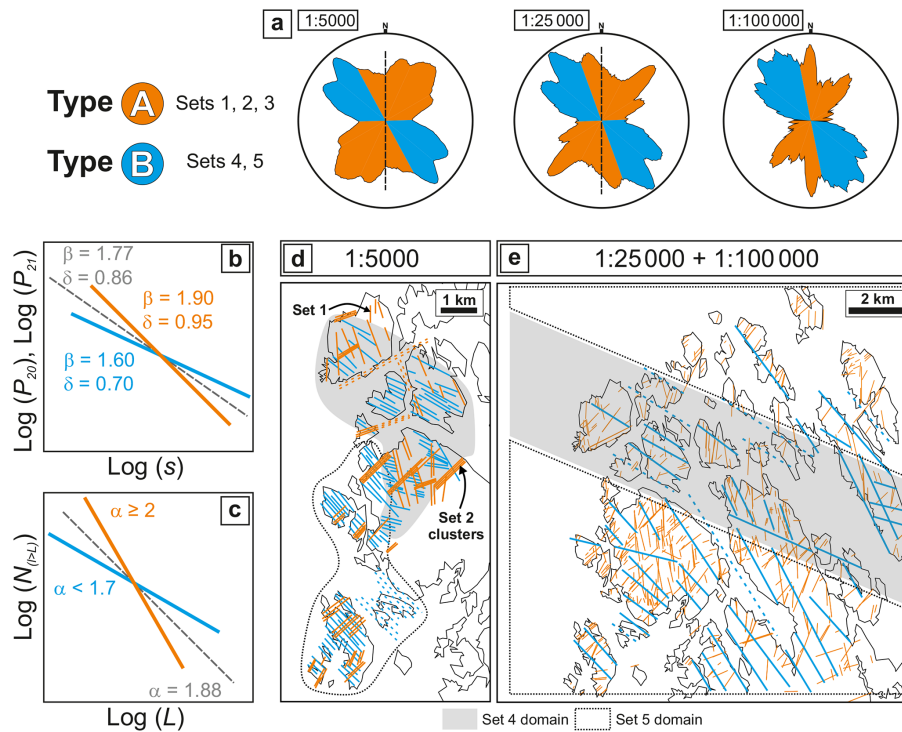
Figure 9. Schematic summary of the results and interpretations for the Rolvsnes granodiorite case study. **(a)** Rose diagrams of the orientation of lineaments at different scales (1 : 5000, 1 : 25 000, 1 : 100 000) with the classification into Type A (Sets 1–3) and B (Sets 4 and 5) lineaments. **(b)** Schematic log-log diagram showing the observed general trends of P_{20} and P_{21} variations with scale. The values of β and δ exponents are reported for the entire lineament network (gray dashed line) and Type A (orange line) and Type B (light blue line) lineaments. **(c)** Schematic log-log diagram showing the observed general scaling laws retrieved for the cumulative length distributions. The values of the exponent α are reported for the entire lineament network (gray dashed line), Type A (orange line) and Type B (light blue line) lineaments. **(d)** Schematic representation of the lineament distribution at 1 : 5000 scale. The reported lineaments are redrawn from the 1 : 5000 lineament map and represent the spatial organization observed within the Rolvsnes granodiorite. **(e)** Schematic representation of the lineament distribution at 1 : 25 000–1 : 100 000 scales. The reported lineaments are redrawn from the 1 : 25 000–1 : 100 000 lineament maps and represent the spatial organization mapped on the Rolvsnes granodiorite. Note the clustered organization of Set 2 lineaments and the two domains (highlighted by transparent gray and dashed areas) where Set 4 and 5 lineaments are dominant.

similar patterns of variation through the scales of observation.

5.1.2 Lineament types within a hierarchical fracture network

For each scale of observation, the box-counting analyses of sub-areas of the lineament maps yielded similar D values (2σ always < 0.1), suggesting that the lineament network is rather homogeneous in space in terms of spatial occupancy. Nonetheless, these results highlight a general decrease in the fractal dimension D from the largest (1 : 100) to the smallest (1 : 100 000) scale of observations (box-and-whisker plots of Fig. 4).

Theoretically, a scale-invariant lineament map should exhibit a similar fractal dimension D irrespective of the scale of observation, of the change in resolution, and of the detail of the lineament maps.

A variation trend in the detected fractal dimensions across scales might, therefore, suggest a change in the spatial occupancy (fractal dimension) of the lineaments detected at the different scales in different proportions. Indeed, the occurrence of lineament orientation sets that are dominant at different scales (local vs. regional scale), showing inherent different spatial occupancy properties (different fractal dimensions of each orientation set), might result in different fractal dimension D values detected at different scales of observation. Accordingly, the observed variation trend of the fractal dimension of the Rolvsnes granodiorite lineament network is consistent with a change in the dominant lineament set orientation and the associated geometrical properties and spatial distribution (see discussion below). In this perspective, the larger D values ($D > 1.45$) at larger scales of observation (1 : 100, 1 : 5000) are consistent with the occurrence of lineament sets more abundant at the local and outcrop scales occupying a larger surface of the maps. Vice versa, the smaller D values ($D < 1.45$) at smaller scales (1 : 25 000, 1 : 100 000)

suggest the occurrence of regional lineaments with a decreased spatial occupancy.

Even if there is a small variability in the fractal dimension D values, none of the measure fractal dimensions, either from small sub-areas or entire lineament maps, are similar to the fractal dimension $D = 1.77$ retrieved from the areal occupancy of the exposed land surface of the Bømlo Island archipelago. The relationship between fractal dimensions of exposed land surface and fracture maps remains to be understood and would deserve further analyses, which however go beyond the scope of the present paper.

The Rolvsnes granodiorite lineament network is composed of five main orientation sets with variable relative abundance, density, and intensity across scales (Figs. 5 and 7 and Table 2). The observed variations in density and intensity are predictable and can be described by a general power-law function, the exponent of which is characteristic of each orientation set (Fig. 7 and Table 5). Even though the single-scale cumulative length distribution for each orientation set can be best approximated by scaling laws other than the power law (Table 3), the multiscale cumulative length distribution is best approximated by a power-law scaling relationship (Fig. 6b and Table 5). Again, each orientation set is characterized by its own power-law exponent (Fig. 6b and Table 5), which differs slightly from that computed for the entire lineament network.

Some lineament sets display similar trends of variation in the relative abundance and intensity, such that they can be grouped into two main set types (Figs. 6b and 9 and Table 5): (1) Type A includes Sets 1–3, characterized by comparable P_{20} and P_{21} variation trends across scales ($\beta \approx 1.90$, $\delta \approx 0.95$) and length distributions ($\alpha \geq 2$), and (2) Type B includes Sets 4 and 5, characterized by comparable P_{20} and P_{21} variation trends across scales ($\beta \approx 1.60$, $\delta \approx 0.70$) and length distributions ($\alpha < 1.7$). This classification into Type A and B lineament sets is not directly reflected in the CoV–V^* diagrams (Fig. 8a and b), the latter rather suggesting a scale-dependent organization of spacing for each lineament set.

Therefore, the observed density–intensity variation and spatial organization trends indicate the occurrence of a hierarchical (scale-dependent) organization of lineament sets within a network presenting overall scale-invariant geometrical properties (e.g., Le Garzic et al., 2011). In this hierarchy, Type B lineaments represent the higher-order structures, controlling the geometrical properties of the network at the regional scale (Fig. 9d and e). Type A lineaments represent lower-order structures and control the geometrical properties of the network at the local-to-outcrop scale (Fig. 9d and e).

At the smallest investigated scale, the homogeneously spaced, WNW-to-NW-striking Type B lineaments (Fig. 9d and e) dominate the network. These lineaments are characteristic of – and predominant over – the whole of onshore western and southwestern Norway (Gabrielsen et al., 2002; Gabrielsen and Braathen, 2014; Tartaglia et al., 2022), as well as offshore (Preiss and Adam, 2021). The power-law exponent for Type B lineaments ($\alpha < 1.7$) suggests that long lineaments represent a substantial part of the overall lineament population. These observations also suggest that Type B lineaments probably result from the homogeneous distribution of deformation at the regional scale, while still representing localized zones accommodating significant deformation at the outcrop scale, when compared to Type A structures (Ackermann et al., 2001). Therefore, these lineaments probably represent major fractures and normal fault zones formed and repeatedly reactivated during the prolonged brittle tectonic history of the Rolvsnes granodiorite (Ceccato et al., 2021a; Preiss and Adam, 2021; Scheiber and Viola, 2018; Viola et al., 2016). The schematic representation of lineaments in Fig. 9d and e highlights a heterogeneous distributions of Type B lineaments, which is not captured by the statistical analysis of spacing heterogeneity. Indeed, the Rolvsnes granodiorite can be subdivided into several domains of the lineament maps where either Set 4 or Set 5 lineaments are predominant at the regional scale ("Set 4–5 domain" – gray and dashed transparent areas in Fig. 9d and e). These domain-type distribution of regional lineaments were already reported by Scheiber and Viola (2018). At the largest analyzed scale, the lineament network is mainly dominated by random-to-clustered, NNW–SSE- to NE–SW-striking Type A lineament sets (Fig. 9d and e). Accordingly, the general power-law exponent ($\alpha \geq 2$) suggests that, among Type A lineaments, short lineaments represent a significant part of that population, probably resulting from an incipient stage of distributed faulting and deformation accommodation (e.g., Ackermann et al., 2001).

5.2 Analysis of reliability, biases, and limitations of the scaling laws

The scaling laws described here have several limitations in their applicability related to (i) occurrence of different orientation sets, (ii) network heterogeneity at different scales, and (iii) analytical biases.

5.2.1 Reliability and biases behind orientation set definitions

The lineament sets defined by this study are grouped in classes based on their azimuthal orientation. As such, they may or may not share a genetic relationship. However, field analyses (Scheiber et al., 2015, 2016; Scheiber and Viola, 2018) have demonstrated the occurrence of systematic sets of fractures, genetically related in terms of chronology, tectonic phase, and orientation, which can be identified from remote sensing techniques. Thus, we assume that the identified orientation sets effectively represent groups of genetically correlated fractures (see below, Sect. 5.3).

The lineament orientation reported by the 1 : 100 rose diagram differs significantly from the orientations of all other

diagrams (Fig. 5). Even though the number of lineaments interpreted from UAV-drone imagery is statistically significant ($N_{Lin} = 930$), the N–S-trending outcrop exposure, its 3D topography, and the location of the exposed area along a major fault zone (Ceccato et al., 2021b, a) are such that it is necessary to question whether the obtained results are truly representative of the larger-scale lineament network. The observed variations in density, intensity, and relative abundance of orientation sets across scales could be affected by several analytical and interpretative orientation-dependent and classification biases.

First of all, under-sampling of specific lineament orientations during manual interpretation may be due to (Scheiber et al., 2015) (i) interpretative biases of the operator, (ii) changes in resolution of the digital representation of the terrain (DTMs and orthophotos) with the changing scale of observation, and (iii) constant direction of the light source adopted for the lidar DTM hill shading (from NW in our study). The change in resolution would equally affect each orientation set, thus maintaining a constant relative abundance across scales. Likely, constant direction of the light source may affect the detection of lineaments at specific orientations, but systematic effects have not been identified by previous studies (Scheiber et al., 2015). Also, the topography, surface extension, perimetral shape, and exposure of outcrops with rough topography (such as the GFZ outcrop analyzed here at 1 : 100 scale) might affect the exposure and detection of specific lineaments and thus orientation sets – some sets may be more visible than others. In particular, gently dipping fractures or fractures parallel to the surface of the outcrop might be underrepresented. Moreover, rose diagrams only report the number of lineaments and do not consider their spatial persistence (length), such that fractures related to the main GFZ and expected to be dominant at the local scale might be represented by very few but longer lineaments. Thus, the small number of lineaments can be diluted and obscured by the large number of short lineaments related to background fracturing.

This notwithstanding, by considering the relative abundance of orientation sets retrieved only from the 1 : 5000, 1 : 25 000, and 1 : 100 000 lineament maps, we can still observe the relative decrease in Sets 1–3 along with the increase in Set 5 lineaments at progressively smaller scales of observation (Fig. 4b). This suggests that the observed variation trends reflect an effective variation in relative abundance of lineaments across scales and represent a real characteristic of the lineament network.

5.2.2 Network vs. orientation set scaling laws

The studied lineament network exhibits some general power-law relationships describing the multiscale behavior of lineament length distribution ($\alpha = 1.88$), density P_{20} ($\beta = 1.77$), and intensity P_{21} ($\delta = 0.86$) (Table 5). These general power-law scaling laws may effectively be adopted to retrieve fracture network properties (geometrical properties and permeability) at any scale of observation. However, the adoption of a general scaling law for the geometrical properties without taking into consideration the peculiarity of each orientation set building up the network may lead to an erroneous extrapolation of the analyzed properties. For example, lineament sets exhibit different power-law exponents for density P_{20} and intensity P_{21} distributions, which, in our case study are systematically smaller for Type A sets and larger for Type B sets than the exponent of the network taken as a whole (Fig. 7). Adopting power-law exponents larger than the actual exponent of the individual lineament set would lead to an overestimation of the network properties at larger scales, and vice versa. In the case of the Rolvsnes granodiorite lineament network, this overestimation or underestimation could be significant and reach 1 order of magnitude in terms of intensity and density (Fig. 7).

5.2.3 Spatial organization and scaling limitations

Field investigations (Ceccato et al., 2021b, a; Scheiber and Viola, 2018) have revealed the highly heterogeneous distribution of fractures at the outcrop scale. Most of the identified fracture sets at the outcrop occur with either a clustered spatial organization or a variable intensity over short distances (50–100 m; Ceccato et al., 2021a). This clearly represents a limitation to the acritical extrapolation of the general power law determined in this study and thus the lower bound for the application of the proposed power-law scaling (Bonnet et al., 2001). Similarly, the "zonal" spatial distribution of Set 4 and 5 lineaments identified at a small scale of observation (see the identified "Set 4 domain" and "Set 5 domain" reported in Fig. 9d and e) needs to be accounted for when evaluating the upper limit of applicability of the general scaling laws defined here. The outcrop-scale spatial heterogeneity and the overestimation–underestimation effects due to applying a general power-law scaling become relevant when considering the role that different fracture sets may have in the definition of the net permeability of a fractured crystalline basement, as highlighted by field studies (Ceccato et al., 2021b, a; Gabrielsen and Braathen, 2014; Torabi et al., 2018).

5.2.4 Analytical biases and statistical methods to overcome them

In the light of the discussion above, it is therefore important to analyze the mapped distributions with appropriate methods and to always consider the regional lineament network as composed of different orientation sets, each of which is characterized by its own geometrical and scaling properties. Additionally, we need to consider all potential sources of error and estimate the analytical and human biases that potentially affect our analyses.

It is worth noting that manual fitting of our multiscale distribution slightly overestimates the power-law exponents re-

trieved from LSR methods (Fig. S2). This might be since LSR methods consider the entire distribution, including the portions of the distributions affected by censoring and truncation, which are inherently excluded by manual fitting.

Most published length datasets and the related fitting results have been analyzed qualitatively (e.g., manual multiscale fitting or LSR of truncated distributions). Indeed, the review process of similar published datasets (for example, particle size distributions) with updated statistical methods has revealed a fundamental misfitting of mathematical distributions and therefore a fundamental misunderstanding of the mathematical function describing the distribution of the investigated geological parameter (Phillips and Williams, 2021). MLE–KS tests have already demonstrated their strength in the analysis of fault attribute distributions (Dichiarante et al., 2020; Kolyukhin and Torabi, 2013). In our case, the results of length cumulative distributions fitting with MLE–KS tests differ significantly from the multiscale LSR power-law relations reported in Fig. 6. Even when the distribution is best approximated by a power-law function (e.g., most lineament sets mapped at 1 : 5000; Table 3), the values of the power-law exponents retrieved from MLE–KS tests ($\alpha > 2.2$) differ from those obtained from the LSR fitting of multiscale distributions ($\alpha < 2.12$).

Even though we might apply very robust statistical methods for the evaluation of the significance of the results of lineament map analyses, we still struggle to accurately quantify the scaling parameters or to define general statistically robust scaling laws. Nevertheless, the first step to improve our accuracy in the quantification of scaling laws and scaling parameters is to consider and discuss the most important biases and analytical errors that might affect the analysis results and lead to deviation from the "natural" scaling laws.

The observed deviations in curve fitting results (both that of single-scale distributions from the power law and that of the single-scale power-law exponents from the multiscale ones) are commonly observed in almost all natural fracture networks. Remarkable deviations from a power-law scaling behavior have been previously explained as resulting from several causes: (i) analytical biases (such as truncation and censoring of lineaments; Dichiarante et al., 2020; Manzocchi et al., 2009; Odling, 1997; Yielding et al., 1996), (ii) subdivision of long lineaments into segments (segmentation; Ackermann et al., 2001; Cao and Lei, 2018; Scholz, 2002; Schultz et al., 2013; Xu et al., 2006), and (iii) effectively different scaling properties at different scales of observation (Castaing et al., 1996; Le Garzic et al., 2011; Kruhl, 2013).

Power-law fitting is usually retrieved from short segments in the central portions of a "truncated" cumulative distribution (e.g., Dichiarante et al., 2020). Truncation and censoring biases may affect large portions (even $> 50\%$ of data) of the cumulative distribution. This would mean that most ($\gg 50\%$ of data) of the analyzed dataset is biased and thus of little use to any kind of statistically significant analysis, such that the related fitting results are not statistically meaningful.

The multiscale distribution analysis can reveal the overarching scaling law of the fracture network and of each lineament set, but the actual values of the exponents of the fitting laws need to be carefully evaluated by also considering the statistical significance of the analyzed dataset.

Segmentation of long lineaments into shorter segments may be due to several causes, both introduced into the dataset by analytical/interpretative biases and intrinsically related to the network topology, fracture chronology, and geological fracture formation processes. Segmentation may result from partial exposure and cover of the fracture network, and it may increase the power-law scaling exponent, without affecting the type of scaling-law function (Cao and Lei, 2018). Segmentation may be related to the progressive growth stages of fault/joint patterns evolving with increasing accommodated deformation and faulting maturity from a network composed of completely isolated short fractures to a network formed by a few long, single lineaments, through fracture interaction and interconnection (Ackermann et al., 2001; Michas et al., 2015; Scholz, 2002). This has been demonstrated to affect both the shape of the mathematical function describing the length distribution (exponential vs. power law) and the power-law exponent at a specific scale of observation (Schultz et al., 2013). However, this may explain the difference in scaling relationships observed during the evolution of a fracture network through time but not at different scales of observation. In addition, the subjective choice of tracing single segments composing a longer lineament as separate fractures rather than tracing a single, continuous, long lineament may likely affect the cumulative length distributions of the fracture network. Tracing single segments would increase the number of short segments compared to longer segments, at constant P_{21} intensity, increasing the total number of traced lineaments and thus increasing the power-law exponent of the distribution (Xu et al., 2006). This segmentation bias may justify the fact that power-law exponents of the LSR multiscale length distributions of each fracture set (Fig. 5b) are systematically smaller than those obtained from single-scale MLE–KS tests at the 1 : 5000 scale. Whether or not this sampling bias may effectively affect the mathematical shape of the cumulative distribution would deserve further investigations, which goes beyond the scope of the present paper.

Thus, the most plausible option is that the fracture network may effectively present different scaling properties at different scales of observations (Kruhl, 2013). Indeed, fault and fracture networks may exhibit a hierarchical organization, which inherently implies scale-dependent geometrical properties and spatial distribution of lineaments (Castaing et al., 1996; Le Garzic et al., 2011). In fact, this is also consistent with the observed variation in relative abundances of orientation sets across scales: each lineament set contributes differently to the overall fracture network geometrical characters, and thus the variation in the relative abundance may also lead to variations in geometrical properties (spatial or-

Table 4. Spacing, CoV, and V^* statistical parameters. The table reports the mean (μ), the standard deviation (σ_S), the minimum and maximum values of spacing (S), CoV, and V^* obtained from scanline statistical analyses.

	s	1 : 5000			1 : 25 000			1 : 100 000		
	Set	S (m)	CoV	V^*	S (m)	CoV	V^*	S (m)	CoV	V^*
		$N_{SL}(N_i > 10) = 17$			$N_{SL}(N_i > 5) = 11$			$N_{SL}(N_i > 3) = 61$		
μ	1a	132.64	0.91	1.45	342.29	0.87	1.77	738.25	0.42	1.40
σ_S		78.55	0.28	0.43	96.80	0.27	0.12	314.96	0.22	0.21
Min		19.37	0.53	0.92	269.18	0.57	1.45	262.68	0.03	1.03
Max		232.39	1.69	2.30	568.70	1.42	1.85	1253.90	0.88	1.80
		$N_{SL}(N_i > 10) = 38$			$N_{SL}(N_i > 5) = 53$			–		
μ	1b	189.33	0.93	1.55	487.49	0.78	1.51	–	–	–
σ_S		52.19	0.18	0.37	175.44	0.23	0.37	–	–	–
Min		87.87	0.57	0.78	133.91	0.25	0.98	–	–	–
Max		311.72	1.44	2.38	883.45	1.25	2.26	–	–	–
		$N_{SL}(N_i > 10) = 47$			$N_{SL}(N_i > 5) = 47$			$N_{SL}(N_i > 3) = 59$		
μ	2	133.39	1.21	1.78	475.32	0.84	1.44	1013.41	0.71	1.52
σ_S		45.48	0.32	0.44	264.12	0.20	0.27	304.75	0.28	0.27
Min		37.64	0.59	1.15	89.24	0.37	0.87	352.64	0.28	1.05
Max		213.61	2.02	2.87	1295.42	1.20	2.12	1506.44	1.31	2.05
		$N_{SL}(N_i > 10) = 22$			$N_{SL}(N_i > 5) = 48$			$N_{SL}(N_i > 3) = 64$		
μ	4	135.66	1.10	1.54	395.51	0.77	1.38	671.34	0.50	1.34
σ_S		41.33	0.29	0.27	183.80	0.26	0.25	403.20	0.26	0.28
Min		75.78	0.57	1.12	81.86	0.31	0.95	150.10	0.04	0.89
Max		251.38	1.62	2.00	804.31	1.51	2.00	1566.48	1.10	1.96
		$N_{SL}(N_i > 10) = 27$			$N_{SL}(N_i > 5) = 77$			$N_{SL}(N_i > 3) = 184$		
μ	5	150.88	0.89	1.36	406.09	0.66	1.27	453.89	0.49	1.23
σ_S		69.94	0.23	0.31	184.59	0.21	0.26	174.28	0.22	0.26
Min		51.16	0.60	0.88	99.05	0.15	0.72	52.05	0.08	0.72
Max		255.16	1.62	2.02	801.94	1.16	1.91	963.48	1.06	1.88

ganization and length distributions) at different scales (e.g., Le Garzic et al., 2011).

5.3 Integration of remote sensing and field observations

The fracture pattern of the Rolvsnes granodiorite includes three main classes of fractures and fault zones (Scheiber et al., 2016; Scheiber and Viola, 2018): (i) pre-Permian, ESE–WNW and NE–SW-striking mineralized shear fractures and minor faults; (ii) Permo-Jurassic major normal faults, mainly striking NW–SE and N–S; and (iii) Cretaceous fracture clusters striking N–S to NNE–SSW.

Smaller normal faults and mineralized shear fractures described by Scheiber and Viola (2018) are subparallel to the lineament Sets 2–4 defined here. They form the background fracture pattern of the Rolvsnes granodiorite (Ceccato et al., 2021a). In particular, Set 4 lineaments are subparallel to the ESE–WNW orientation of the (relatively) oldest generation of fractures identified in the field (Scheiber and Viola, 2018).

Indeed, the regional distribution of Set 4 and the geometrical characteristics discussed above stress their importance as regional structures accommodating significant deformation through the brittle deformation history of the Rolvsnes granodiorite (Scheiber and Viola, 2018). Conversely, NE–SW minor faults and shear fractures, subparallel to Set 2 and 3 lineaments, accommodated only limited deformation, which may be compatible with their local-scale distribution and geometrical characteristics (e.g., Ackermann et al., 2001). Permo-Jurassic normal fault zones are oriented NW–SE to N–S, similarly to our Set 5 and Set 1(b) lineaments. The geometrical characters and spatial distribution of Set 5 lineaments suggest their role as important zones of deformation accommodation at the regional scale. N–S to NNE–SSW fracture clusters are comparable to Set 1(a) orientations; they are indeed local-scale structural features and are inferred to have accommodated limited deformation during Cretaceous rifting of the North Sea (Scheiber and Viola, 2018).

Table 5. Summary table reporting the power-law scaling and the values of the related parameters retrieved from the multiscale analysis of cumulative length distribution, lineament density, and intensity.

| | | Cumulative length distributions | | | P_{20} density distribution | | | P_{21} intensity distribution | | |
| | | $N_{(l>L)} = m \cdot L^{-\alpha}$ | | | $P_{20} = m \cdot s^{-\beta}$ | | | $P_{21} = m \cdot s^{-\delta}$ | | |
	Set Type	m	α	R^2	m	β	R^2	m	δ	R^2
Set 1	A	0.074	1.99	0.610	475	1.83	0.992	15.7	0.92	0.997
Set 2	A	0.146	2.21	0.552	761	1.88	0.988	30.6	1.01	0.979
Set 3	A	0.025	1.99	0.677	371	1.96	0.999	9.4	1.04	0.999
Set 4	B	0.019	1.67	0.678	76	1.66	0.994	1.9	0.74	0.992
Set 5	B	0.022	1.62	0.679	50	1.58	0.982	1.4	0.64	0.967
Total		0.261	1.88	0.594	1187	1.77	0.989	37.6	0.86	0.986

Summarizing, although our lineament classification in Types A and B is certainly an oversimplification of the actual complexity of the natural fracture network, it provides valuable information as to the geometrical characteristics of faults and fractures and their regional and local importance as zones of deformation accommodation.

5.3.1 Constraints on the multiscale permeability structure of crystalline basement

As constrained by field studies, each lineament/fracture set may contribute differently to the bulk permeability of a fractured crystalline basement block (Ceccato et al., 2021b, a; Gabrielsen and Braathen, 2014; Torabi et al., 2018). The effects of the background fracturing of the Rolvsnes granodiorite on permeability is secondary (Ceccato et al., 2021a), it being mainly composed of minor sealed faults and mineralized fractures belonging to Set 2–4 lineaments. It is the regional-scale structures, like our Type B lineaments (Set 5; e.g., the GFZ), that effectively control permeability, fluid flow, and reservoir compartmentalization at the regional scale (Ceccato et al., 2021a; Holdsworth et al., 2019). Results from in situ petrophysical analyses and discrete fracture network modeling of fault zone permeability have shown that these structures behave as a mixed conduit–barrier for fluid flow, and they are characterized by a strongly anisotropic permeability tensor (Caine et al., 1996; Ceccato et al., 2021a). Fluid flow is promoted parallel to the main fault plane, especially parallel to the (sub-horizontal) intersection directions of the dominant fracture sets within the fault damage zone, whereas the anisotropic permeability of the fault core brittle structural facies buffers cross-fault fluid flow (Ceccato et al., 2021b, a; Tartaglia et al., 2020). Conversely, fracture clusters, comparable to our Set 1(a) lineaments, may represent effective fluid pathways at the outcrop scale, acting as preferential conduits for vertical fluid flow within the basement (Ceccato et al., 2021b, a; Torabi et al., 2018; Place et al., 2016; Souque et al., 2019).

In summary, by integrating field and remote sensing data, we can improve the conceptual models and their dimen-

sioning in an attempt to describe the anisotropic permeability structure of a fractured crystalline basement at different scales (e.g., Fig. 11 of Ceccato et al., 2021b). Our results constrain the heterogeneous structure of a fractured basement block in terms of orientation and spatial distribution of permeability. The permeability of the fractured basement at the regional scale is characterized by the occurrence of rhombohedral-shaped compartments (the fault-bounded polygonal domains of Ceccato et al., 2021b) that are homogeneously distributed and defined by the higher-hierarchical-order Type B lineaments. Their extension is determined by the spacing of Type B lineaments, ranging on the order of 500–1000 m at the regional scale (Table 4). Fluid flow is promoted along the major fault planes and parallel to the sub-horizontal intersections of fracture sets dominant within the fault damage zones (Ceccato et al., 2021a). Within these rhombohedral compartments, permeability is heterogeneously distributed at the 50–100 m scale, following the random-to-uniform spacing distribution of lower-hierarchical-order Type A (Set 1b) lineaments (Table 4). At the outcrop scale, these N–S lineaments are represented by fracture clusters, which promote vertical fluid flow (Ceccato et al., 2021b, a).

Accordingly, any underestimation and/or overestimation of spatial distribution and density of the lineaments may deeply affect the accuracy of hydrological and petrophysical models of fractured basement blocks at the outcrop and at the sub-seismic resolution scale (Bertrand et al., 2015; Le Garzic et al., 2011).

6 Conclusions

The fractured crystalline basement of the Rolvsnes granodiorite on Bømlo is characterized by the occurrence of a fractal fracture network controlled by a general power-law scaling law for the distribution of fracture lengths. However, detailed orientation-dependent analyses have revealed that this first-approximation scale-invariant lineament network is composed of lineament sets, which individually exhibit a

scale-dependent hierarchical spatial distribution, and parameter variation trends with the scale of observation. Different trends of intensity–density variation across scales for each orientation set have been detected, as well as different scaling laws for length distribution of each orientation set. These results, integrated with field observations, suggest that the documented lineament network results from the summation of different geological structures (e.g., faults vs. joints, major fault zones vs. incipient minor faults) organized in a hierarchical manner and characterized by different geometrical and scale-dependent properties.

The hierarchical lineament network affecting the Rolvsnes granodiorite controls the anisotropy and directionality of the permeability structure of the basement at different scales. At the regional scale, the crystalline basement is characterized by a rhombohedral pattern of basement compartments bounded by regional fault zones impermeable to cross-fault fluid flow. Within these compartments, the permeability structure is controlled by local-scale fracture clusters, promoting subvertical N–S-striking fluid flow.

Our study allows us to draw some general conclusions about the methods for characterization of fracture network and their analysis.

– Firstly, the presented multiscale analytical workflow may represent a valid option for the quantification of large, inherently incomplete (due to analytical and subjective biases) lineament datasets. The lineament maps retrieved from digital terrain and surface models of the Rolvsnes granodiorite offer very large datasets, which are inherently incomplete due to partial exposure and/or incomplete sampling of lineament due to partial exposure, resolution, or human biases. Thus, a statistical approach such as that proposed in this paper is highly recommended when aiming to retrieve relevant information from datasets that, for several reasons, are only partially representative for the entire fracture network.

– Detailed orientation-dependent multiscale analyses of the lineament network can provide the different scaling laws and geometrical properties for each constituent lineament set, which can be adopted to improve the detail and tune the accuracy of permeability models of fractured crystalline basements considering outcrop-scale structural features.

– The integration of multiscale length distribution analyses, multiscale intensity–density estimations, and multiscale description of spatial organization provides useful information for the classification of topographic lineaments as different geological structures (e.g., fracture clusters vs. fault zones) with specific hierarchy and control on the permeability of the fractured basement.

Author contributions. AC, GT, MA, and GV initially conceptualized the study. AC and GT performed the lineament mapping. AC developed and performed the statistical analyses and data curation. AC prepared the original paper draft and figures. AC, GT, MA, and GV contributed to the final version of the paper.

References

Achtziger-Zupančič, P., Loew, S., and Mariéthoz, G.: A new global database to improve predictions of permeability distribution in crystalline rocks at site scale, J. Geophys. Res.-Sol. Ea., 122, 3513–3539, https://doi.org/10.1002/2017JB014106, 2017.

Ackermann, R. V., Schlische, R. W., and Withjack, M. O.: The geometric and statistical evolution of normal fault systems: an experimental study of the effects of mechanical layer

thickness on scaling laws, J. Struct. Geol., 23, 1803–1819, https://doi.org/10.1016/S0191-8141(01)00028-1, 2001.

Andrews, B. J., Roberts, J. J., Shipton, Z. K., Bigi, S., Tartarello, M. C., and Johnson, G.: How do we see fractures? Quantifying subjective bias in fracture data collection, Solid Earth, 10, 487–516, https://doi.org/10.5194/se-10-487-2019, 2019.

Bell, R. E., Jackson, C. A. L., Whipp, P. S., and Clements, B.: Strain migration during multiphase extension: Observations from the northern North Sea, Tectonics, 33, 1936–1963, https://doi.org/10.1002/2014TC003551, 2014.

Bertrand, L., Géraud, Y., Le Garzic, E., Place, J., Diraison, M., Walter, B., and Haffen, S.: A multiscale analysis of a fracture pattern in granite: A case study of the Tamariu granite, Catalunya, Spain, J. Struct. Geol., 78, 52–66, https://doi.org/10.1016/j.jsg.2015.05.013, 2015.

Bistacchi, A., Mittempergher, S., Martinelli, M., and Storti, F.: On a new robust workflow for the statistical and spatial analysis of fracture data collected with scanlines (or the importance of stationarity), Solid Earth, 11, 2535–2547, https://doi.org/10.5194/se-11-2535-2020, 2020.

Bonnet, E., Bour, O., Odling, N. E., Davy, P., Main, I., Cowie, P., and Berkowitz, B.: Scaling of fracture systems in geological media, Rev. Geophys., 39, 347–383, 2001.

Bossennec, C., Frey, M., Seib, L., Bär, K., and Sass, I.: Multiscale characterisation of fracture patterns of a crystalline reservoir analogue, Geosciences, 11, 1–23, https://doi.org/10.3390/geosciences11090371, 2021.

Bossennec, C., Seib, L., Frey, M., van der Vaart, J., and Sass, I.: Structural Architecture and Permeability Patterns of Crystalline Reservoir Rocks in the Northern Upper Rhine Graben: Insights from Surface Analogues of the Odenwald, Energies, 15, 1310, https://doi.org/10.3390/EN15041310, 2022.

Bour, O., Davy, P., Darcel, C., and Odling, N.: A statistical scaling model for fracture network geometry, with validation on a multiscale mapping of a joint network (Hornelen Basin, Norway), J. Geophys. Res.-Sol. Ea., 107, ETG 4-1, https://doi.org/10.1029/2001JB000176, 2002.

Brace, W. F.: Permeability of Crystalline Rocks: New in Situ Measurements, J. Geophys. Res., 89, 4327–4330, https://doi.org/10.1029/jb089ib06p04327, 1984.

Caine, J. S. and Tomusiak, S. R. A.: Brittle structures and their role in controlling porosity and permeability in a complex Precambrian crystalline-rock aquifer system in the Colorado Rocky Mountain Front Range, GSA Bull., 115, 1410–1424, https://doi.org/10.1130/B25088.1, 2003.

Caine, J. S., Evans, J. P., and Forster, C. B.: Fault zone architecture and permeability structure, Geology, 24, 1025–1028, https://doi.org/10.1130/0091-7613(1996)024<1025:FZAAPS>2.3.CO;2, 1996.

Cao, W. and Lei, Q.: Influence of Landscape Coverage on Measuring Spatial and Length Properties of Rock Fracture Networks: Insights from Numerical Simulation, Pure Appl. Geophys., 175, 2167–2179, https://doi.org/10.1007/s00024-018-1774-4, 2018.

Castaing, C., Halawani, M. A., Gervais, F., Chilès, J. P., Genter, A., Bourgine, B., Ouillon, G., Brosse, J. M., Martin, P., Genna, A., and Janjou, D.: Scaling relationships in intraplate fracture systems related to Red Sea rifting, Tectonophysics, 261, 291–314, https://doi.org/10.1016/0040-1951(95)00177-8, 1996.

Ceccato, A., Viola, G., Antonellini, M., Tartaglia, G., and Ryan, E. J.: Constraints upon fault zone properties by combined structural analysis of virtual outcrop models and discrete fracture network modelling, J. Struct. Geol., 152, 104444, https://doi.org/10.1016/j.jsg.2021.104444, 2021a.

Ceccato, A., Viola, G., Tartaglia, G., and Antonellini, M.: In–situ quantification of mechanical and permeability properties on outcrop analogues of offshore fractured and weathered crystalline basement: Examples from the Rolvsnes granodiorite, Bømlo, Norway, Mar. Petrol. Geol., 124, 104859, https://doi.org/10.1016/j.marpetgeo.2020.104859, 2021b.

Ceccato, A., Tartaglia, G., Antonellini, M., and Viola, G.: "Online Data Repository for Ceccato et al. 2022 – SolidEarth", Mendeley Data [data set], V1, https://doi.org/10.17632/3ymhkpmr9s.1, 2022.

Chabani, A., Trullenque, G., Ledésert, B. A., and Klee, J.: Multiscale characterization of fracture patterns: A case study of the noble hills range (Death valley, CA, USA), application to geothermal reservoirs, Geosciences, 11, 25–27, https://doi.org/10.3390/geosciences11070280, 2021.

Davy, P., Bour, O., De Dreuzy, J. R., and Darcel, C.: Flow in multi-scale fractal fracture networks, Geol. Soc. Spec. Publ., 261, 31–45, https://doi.org/10.1144/GSL.SP.2006.261.01.03, 2006.

Dershowitz, W. S. and Herda, H. H.: Interpretation of fracture spacing and intensity. The 33rd U. S. Symposium on Rock Mechanics (USRMS), Santa Fe, New Mexico, June 1992, 757–766, http://onepetro.org/ARMAUSRMS/proceedings-pdf/ARMA92/All-ARMA92/ARMA-92-0757/1987502/arma-92-0757.pdf (last access: 6 September 2022), 1992.

Dichiarante, A. M., McCaffrey, K. J. W., Holdsworth, R. E., Bjørnarå, T. I., and Dempsey, E. D.: Fracture attribute scaling and connectivity in the Devonian Orcadian Basin with implications for geologically equivalent sub-surface fractured reservoirs, Solid Earth, 11, 2221–2244, https://doi.org/10.5194/se-11-2221-2020, 2020.

Evans, J. P., Forster, C. B., and Goddard, J. V.: Permeability of fault-related rocks, and implications for hydraulic structure of fault zones, J. Struct. Geol., 19, 1393–1404, https://doi.org/10.1016/S0191-8141(97)00057-6, 1997.

Fossen, H., Khani, H. F., Faleide, J. I., Ksienzyk, A. K., and Dunlap, W. J.: Post-Caledonian extension in the West Norway–northern North Sea region: the role of structural inheritance, Geol. Soc. London Spec. Publ., 439, 465–486, https://doi.org/10.1144/SP439.6, 2017.

Fossen, H., Ksienzyk, A. K., Rotevatn, A., Bauck, M. S., and Wemmer, K.: From widespread faulting to localised rifting: Evidence from K-Ar fault gouge dates from the Norwegian North Sea rift shoulder, Basin Res., 33, 1934–1953, https://doi.org/10.1111/BRE.12541/CITE/REFWORKS, 2021.

Fredin, O., Viola, G., Zwingmann, H., Sørlie, R., Brönner, M., Lie, J. E., Grandal, E. M., Müller, A., Margreth, A., Vogt, C., and Knies, J.: The inheritance of a mesozoic landscape in western Scandinavia, Nat. Commun., 8, 14879, https://doi.org/10.1038/ncomms14879, 2017.

Gabrielsen, R. H. and Braathen, A.: Models of fracture lineaments – Joint swarms, fracture corridors and faults in crystalline rocks, and their genetic relations, Tectonophysics, 628, 26–44, https://doi.org/10.1016/j.tecto.2014.04.022, 2014.

Gabrielsen, R. H., Braathen, A., Dehis, J., and Roberts, D.: Tectonic lineaments of Norway, Norsk Geol. Tidsskr., 82, 153–174, 2002.

Gee, D. G., Fossen, H., Henriksen, N., and Higgins, A. K.: From the Early Paleozoic Platforms of Baltica and Laurentia to the Caledonide Orogen of Scandinavia and Greenland, Episodes, 31, 44–51, https://doi.org/10.18814/EPIIUGS/2008/V31I1/007, 2008.

Gillespie, P. A., Howard, C. B., Walsh, J. J., and Watterson, J.: Measurement and characterisation of spatial distributions of fractures, Tectonophysics, 226, 113–141, https://doi.org/10.1016/0040-1951(93)90114-Y, 1993.

Gillespie, P. A., Walsh, J. J., Watterson, J., Bonson, C. G., and Manzocchi, T.: Scaling relationships of joint and vein arrays from The Burren, Co. Clare, Ireland, J. Struct. Geol., 23, 183–201, https://doi.org/10.1016/S0191-8141(00)00090-0, 2001.

Hardebol, N. J., Maier, C., Nick, H., Geiger, S., Bertotti, G., and Boro, H.: Multiscale fracture network characterization and impact on flow: A case study on the Latemar carbonate platform, J. Geophys. Res.-Sol. Ea., 120, 8197–8222, https://doi.org/10.1002/2015JB011879, 2015.

Healy, D., Rizzo, R. E., Cornwell, D. G., Farrell, N. J. C., Watkins, H., Timms, N. E., Gomez-Rivas, E., and Smith, M.: FracPaQ: A MATLAB^{TM} toolbox for the quantification of fracture patterns, J. Struct. Geol., 95, 1–16, https://doi.org/10.1016/j.jsg.2016.12.003, 2017.

Hirata, T.: Fractal Dimension of Fault Systems in Japan: Fractal Structure in Rock Fracture Geometry at Various Scales, Fractals Geophys., 131, 157–170, https://doi.org/10.1007/978-3-0348-6389-6_9, 1989.

Holdsworth, R. E., McCaffrey, K. J. W., Dempsey, E., Roberts, N. M. W., Hardman, K., Morton, A., Feely, M., Hunt, J., Conway, A., and Robertson, A.: Natural fracture propping and earthquake-induced oil migration in fractured basement reservoirs, Geology, 47, 700–704, https://doi.org/10.1130/G46280.1, 2019.

Kolyukhin, D. and Torabi, A.: Power-Law Testing for Fault Attributes Distributions, Pure Appl. Geophys., 170, 2173–2183, https://doi.org/10.1007/s00024-013-0644-3, 2013.

Kruhl, J. H.: Fractal-geometry techniques in the quantification of complex rock structures: A special view on scaling regimes, inhomogeneity and anisotropy, J. Struct. Geol., 46, 2–21, https://doi.org/10.1016/j.jsg.2012.10.002, 2013.

Le Garzic, E., de L'Hamaide, T., Diraison, M., Géraud, Y., Sausse, J., de Urreiztieta, M., Hauville, B., and Champanhet, J. M.: Scaling and geometric properties of extensional fracture systems in the proterozoic basement of Yemen. Tectonic interpretation and fluid flow implications, J. Struct. Geol., 33, 519–536, https://doi.org/10.1016/j.jsg.2011.01.012, 2011.

Lundmark, A. M., Sæther, T., and Sørlie, R.: Ordovician to silurian magmatism on the Utsira High, North Sea: Implications for correlations between the onshore and offshore Caledonides, Geol. Soc. Spec. Publ., 390, 513–523, https://doi.org/10.1144/SP390.21, 2014.

Manzocchi, T., Walsh, J. J., and Bailey, W. R.: Population scaling biases in map samples of power-law fault systems, J. Struct. Geol., 31, 1612–1626, https://doi.org/10.1016/j.jsg.2009.06.004, 2009.

Marrett, R., Gale, J. F. W., Gómez, L. A., and Laubach, S. E.: Correlation analysis of fracture arrangement in space, J. Struct. Geol., 108, 16–33, https://doi.org/10.1016/j.jsg.2017.06.012, 2018.

McCaffrey, K. J. W., Holdsworth, R. E., Pless, J., Franklin, B. S. G., and Hardman, K.: Basement reservoir plumbing: fracture aperture, length and topology analysis of the Lewisian Complex, NW Scotland, J. Geol. Soc. London, 177, 1281–1293, https://doi.org/10.1144/jgs2019-143, 2020.

Michas, G., Vallianatos, F., and Sammonds, P.: Statistical mechanics and scaling of fault populations with increasing strain in the Corinth Rift, Earth Planet. Sc. Lett., 431, 150–163, https://doi.org/10.1016/J.EPSL.2015.09.014, 2015.

Munro, M. A. and Blenkinsop, T. G.: MARD-A moving average rose diagram application for the geosciences, Comput. Geosci., 49, 112–120, https://doi.org/10.1016/j.cageo.2012.07.012, 2012.

Nyberg, B., Nixon, C. W., and Sanderson, D. J.: NetworkGT: A GIS tool for geometric and topological analysis of two-dimensional fracture networks, Geosphere, 14, 1618–1634, https://doi.org/10.1130/GES01595.1, 2018.

Odling, N. E.: Scaling and connectivity of joint systems in sandstones from western Norway, J. Struct. Geol., 19, 1257–1271, https://doi.org/10.1016/S0191-8141(97)00041-2, 1997.

Odling, N. E., Gillespie, P., Bourgine, B., Castaing, C., Chiles, J. P., Christensen, N. P., and Watterson, J.: Variations in fracture system geometry and their implications for fluid flow in fractures hydrocarbon reservoirs, Petrol. Geosci., 5, 373–384, https://doi.org/10.1144/petgeo.5.4.373, 1999.

Peacock, D. C. P. and Sanderson, D. J.: Structural analyses and fracture network characterisation: Seven pillars of wisdom, Earth-Sci. Rev., 184, 13–28, https://doi.org/10.1016/j.earscirev.2018.06.006, 2018.

Peacock, D. C. P., Sanderson, D. J., Bastesen, E., Rotevatn, A., and Storstein, T. H.: Causes of bias and uncertainty in fracture network analysis, Norw. J. Geol., 99, 1–16, https://doi.org/10.17850/njg99-1-06, 2019.

Pennacchioni, G., Ceccato, A., Fioretti, A. M., Mazzoli, C., Zorzi, F., and Ferretti, P.: Episyenites in meta-granitoids of the Tauern Window (Eastern Alps): unpredictable?, J. Geodyn., 101, 73–87, https://doi.org/10.1016/j.jog.2016.04.001, 2016.

Phillips, N. J. and Williams, R. T.: To D or not to D? Re-evaluating particle-size distributions in natural and experimental fault rocks, Earth Planet. Sc. Lett., 553, 116635, https://doi.org/10.1016/J.EPSL.2020.116635, 2021.

Place, J., Géraud, Y., Diraison, M., Herquel, G., Edel, J. B., Bano, M., Le Garzic, E., and Walter, B.: Structural control of weathering processes within exhumed granitoids: Compartmentalisation of geophysical properties by faults and fractures, J. Struct. Geol., 84, 102–119, https://doi.org/10.1016/j.jsg.2015.11.011, 2016.

Preiss, A. D. and Adam, J.: Basement fault trends in the Southern North Sea Basin, J. Struct. Geol., 153, 104449, https://doi.org/10.1016/J.JSG.2021.104449, 2021.

Rizzo, R. E., Healy, D., and De Siena, L.: Benefits of maximum likelihood estimators for fracture attribute analysis: Implications for permeability and up-scaling, J. Struct. Geol., 95, 17–31, https://doi.org/10.1016/j.jsg.2016.12.005, 2017.

Sanderson, D. J. and Peacock, D. C. P.: Line sampling of fracture swarms and corridors, J. Struct. Geol., 122, 27–37, https://doi.org/10.1016/j.jsg.2019.02.006, 2019.

Scheiber, T. and Viola, G.: Complex Bedrock Fracture Patterns: A Multipronged Approach to Resolve Their Evolution in Space and Time, Tectonics, 37, 1030–1062, https://doi.org/10.1002/2017TC004763, 2018.

Scheiber, T., Fredin, O., Viola, G., Jarna, A., Gasser, D., and Łapińska-Viola, R.: Manual extraction of bedrock lineaments from high-resolution LiDAR data: methodological bias and human perception, GFF, 137, 362–372, https://doi.org/10.1080/11035897.2015.1085434, 2015.

Scheiber, T., Viola, G., Wilkinson, C. M., Ganerød, M., Skår, Ø., and Gasser, D.: Direct ^{40}Ar/^{39}Ar dating of Late Ordovician and Silurian brittle faulting in the southwestern Norwegian Caledonides, Terra Nova, 28, 374–382, https://doi.org/10.1111/TER.12230, 2016.

Schneeberger, R., Egli, D., Lanyon, G. W., Mäder, U. K., Berger, A., Kober, F., and Herwegh, M.: Structural-permeability favorability in crystalline rocks and implications for groundwater flow paths: a case study from the Aar Massif (central Switzerland), Hydrogeol. J., 26, 2725–2738, https://doi.org/10.1007/s10040-018-1826-y, 2018.

Scholz, C. H.: The Mechanics of Earthquakes and Faulting, 2nd edn., Cambridge University Press, https://doi.org/10.1017/CBO9780511818516, 2002.

Schultz, R. A., Klimczak, C., Fossen, H., Olson, J. E., Exner, U., Reeves, D. M., and Soliva, R.: Statistical tests of scaling relationships for geologic structures, J. Struct. Geol., 48, 85–94, https://doi.org/10.1016/J.JSG.2012.12.005, 2013.

Slagstad, T., Davidsen, B., and Stephen Daly, J.: Age and composition of crystalline basement rocks on the norwegian continental margin: Offshore extension and continuity of the Caledonian-Appalachian orogenic belt, J. Geol. Soc. London, 168, 1167–1185, https://doi.org/10.1144/0016-76492010-136, 2011.

Souque, C., Knipe, R. J., Davies, R. K., Jones, P., Welch, M. J., and Lorenz, J.: Fracture corridors and fault reactivation: Example from the Chalk, Isle of Thanet, Kent, England, J. Struct. Geol., 122, 11–26, https://doi.org/10.1016/j.jsg.2018.12.004, 2019.

Stephens, M. A.: Use of the Kolmogorov–Smirnov, Cramér–Von Mises and Related Statistics Without Extensive Tables, J. Roy. Stat. Soc. B Met., 32, 115–122, https://doi.org/10.1111/J.2517-6161.1970.TB00821.X, 1970.

Stober, I. and Bucher, K.: Hydraulic conductivity of fractured upper crust: Insights from hydraulic tests in boreholes and fluid-rock interaction in crystalline basement rocks, Geofluids, 15, 161–178, https://doi.org/10.1111/gfl.12104, 2015.

Tartaglia, G., Viola, G., van der Lelij, R., Scheiber, T., Ceccato, A., and Schönenberger, J.: "Brittle structural facies" analysis: A diagnostic method to unravel and date multiple slip events of long-lived faults, Earth Planet. Sc. Lett., 545, 116420, https://doi.org/10.1016/j.epsl.2020.116420, 2020.

Tartaglia, G., Ceccato, A., Scheiber, T., van der Lelij, R., Schönenberger, J., and Viola, G.: Time-constrained multiphase brittle tectonic evolution of the onshore mid-Norwegian passive margin, GSA Bull., 1–22, https://doi.org/10.1130/b36312.1, 2022.

Torabi, A. and Berg, S. S.: Scaling of fault attributes: A review, Mar. Petrol. Geol., 28, 1444–1460, https://doi.org/10.1016/j.marpetgeo.2011.04.003, 2011.

Torabi, A., Alaei, B., and Ellingsen, T. S. S.: Faults and fractures in basement rocks, their architecture, petrophysical and mechanical properties, J. Struct. Geol., 117, 256–263, https://doi.org/10.1016/J.JSG.2018.07.001, 2018.

Trice, R., Hiorth, C., and Holdsworth, R.: Fractured basement play development on the UK and Norwegian rifted margins, Geol. Soc. London Spec. Publ., SP495-2018-174, 495, https://doi.org/10.1144/sp495-2018-174, 2019.

Viola, G., Scheiber, T., Fredin, O., Zwingmann, H., Margreth, A., and Knies, J.: Deconvoluting complex structural histories archived in brittle fault zones, Nat. Commun., 71, 1–10, https://doi.org/10.1038/ncomms13448, 2016.

Xu, S. S., Nieto-Samaniego, A. F., Alaniz-Álvarez, S. A., and Velasquillo-Martínez, L. G.: Effect of sampling and linkage on fault length and length-displacement relationship, Int. J. Earth Sci., 95, 841–853, https://doi.org/10.1007/s00531-005-0065-3, 2006.

Yielding, G., Needham, T., and Jones, H.: Sampling of fault populations using sub-surface data: A review, J. Struct. Geol., 18, 135–146, https://doi.org/10.1016/S0191-8141(96)80039-3, 1996.